

# Applications of thin-film lithium niobate in nonlinear integrated photonics

Milad Gholipour Vazimali<sup>a</sup> and Sasan Fathpour<sup>a,b,\*</sup>

<sup>a</sup>University of Central Florida, CREOL, College of Optics and Photonics, Orlando, Florida, United States

<sup>b</sup>University of Central Florida, Department of Electrical and Computer Engineering, Orlando, Florida, United States

**Abstract.** Photonics on thin-film lithium niobate (TFLN) has emerged as one of the most pursued disciplines within integrated optics. Ultracompact and low-loss optical waveguides and related devices on this modern material platform have rejuvenated the traditional and commercial applications of lithium niobate for optical modulators based on the electro-optic effect, as well as optical wavelength converters based on second-order nonlinear effects, e.g., second-harmonic, sum-, and difference-frequency generations. TFLN has also created vast opportunities for applications and integrated solutions for optical parametric amplification and oscillation, cascaded nonlinear effects, such as low-harmonic generation; third-order nonlinear effects, such as supercontinuum generation; optical frequency comb generation and stabilization; and nonclassical nonlinear effects, such as spontaneous parametric downconversion for quantum optics. Recent progress in nonlinear integrated photonics on TFLN for all these applications, their current trends, and future opportunities and challenges are reviewed.

Keywords: lithium niobate; thin-film lithium niobate; nonlinear integrated optics; photonic integrated circuits.

Received Mar. 15, 2022; revised manuscript received Apr. 13, 2022; accepted for publication May 3, 2022; published online May 30, 2022.

© The Authors. Published by SPIE and CLP under a Creative Commons Attribution 4.0 International License. Distribution or reproduction of this work in whole or in part requires full attribution of the original publication, including its DOI.

[DOI: [10.1117/1.AP.4.3.034001](https://doi.org/10.1117/1.AP.4.3.034001)]

## 1 Introduction

The excellent electro-optic (EO) and nonlinear optical properties of lithium niobate ( $\text{LiNbO}_3$  or LN) have long established it as a prevailing photonic material for the long-haul telecom modulator and wavelength-converter markets. Indeed, the first nonlinear experiment in any waveguide platform was a demonstration of Cherenkov radiation from titanium-diffused LN.<sup>1</sup> Conventional LN waveguides are most commonly formed by in-diffusion of titanium (Ti) dopants<sup>2</sup> or by the proton exchange process.<sup>3</sup> However, these conventional lithium niobate optical waveguides have a low index-contrast, hence are bulky compared with modern integrated platforms, such as silicon photonics. The bulkiness impedes photonic circuit implementations and imposes high optical power requirements for nonlinear applications.

Achieving thin films of LN (with a thickness of a few hundred nanometers) that reside on an insulator cladding with a much lower index (e.g., silicon dioxide,  $\text{SiO}_2$ )—along with

methods to achieve low-loss ridge or channel waveguides on the thin films—can address the above issues and yield high-contrast waveguides. Thin-film lithium niobate (TFLN) wafers on silicon (Si) substrates and high-contrast waveguides (with submicron cross-sectional dimensions) were developed for the first time at CREOL in 2013.<sup>4</sup> Since the commercialization of TFLN wafers by a few vendors,<sup>5–7</sup> efforts by several research teams have tremendously advanced the field of TFLN-integrated photonics. A plethora of ultracompact linear and nonlinear optical devices and circuits (waveguides, microring resonators, modulators, grating couplers, wavelength converters, entangled photon sources, isolators, supercontinuum, and comb sources) with unprecedented or significantly superior performances than the conventional (bulk) LN counterparts have been demonstrated. The combined efforts have rejuvenated LN for EO, nonlinear-, and quantum-optics applications, and the material is considered to be among the top candidates for heterogeneous integrated photonics. That is when multiple materials are monolithically integrated on the same substrate (preferably silicon), while each material is chosen for the functionalities that it suits the best.

\*Address all correspondence to Sasan Fathpour, [fathpour@creol.ucf.edu](mailto:fathpour@creol.ucf.edu)

TFLN is still under investigation for a better understanding of its fundamental properties, such as crystal defects, optical damage,<sup>8</sup> and the photorefractive effect.<sup>9</sup> First-principle studies have also been used to explore new capabilities of the material.<sup>10,11</sup> Dry etching of LN is challenging in bulky conventional waveguides with deep sidewalls, hence diffusion or implantation of dopants is typically preferred. Etching appeared to be challenging in the early years of TFLN, thus rib-loading techniques were adopted,<sup>4,12,13</sup> which is indeed advantageous for EO devices in some respects.<sup>14</sup> However, direct etching of LN is preferred for nonlinear-optic applications. Partially due to the shallow etching required in TFLN waveguides, optical propagation losses as low as 0.027 dB/cm,<sup>15</sup> as well as intrinsic  $Q$ -factors beyond  $10^8$ ,<sup>16</sup> have been achieved. Even at the wafer level, a propagation loss of 0.27 dB/cm has been demonstrated,<sup>17</sup> which is an important milestone for large-scale integration. Progress in fabrication processes on TFLN is reviewed elsewhere.<sup>18,19</sup>

Numerous studies have also been conducted on the technological improvement of the platform such as domain engineering,<sup>18,20–23</sup> which is particularly important for nonlinear devices based on periodic poling. Increasing numbers of functionalities are being demonstrated on TFLN and are rendering it a fully functional integrated platform. For example, light sources including rare-earth ion-doped<sup>24–29</sup> and Raman lasers<sup>30,31</sup> as well as heterogeneously integrated electrically pumped III-V lasers<sup>32,33</sup> have been demonstrated. Shams et al.<sup>33</sup> adopted flip-chip bonding and demonstrated electrically pumped DFB lasers on TFLN with up to 60 mW of optical power coupled to the TFLN waveguide. The performance of EO modulators is still being further improved,<sup>34,35</sup> with a recently reported data transmission rate of 1.96 Tb/s at a single wavelength with a 110 GHz 3-dB bandwidth and <1 V of driving voltage.<sup>36</sup> Progress has been made in design and experimental results to enhance the EO bandwidth of TFLN modulators into the subterahertz regime.<sup>14,37</sup> Other components, such as highly efficient couplers,<sup>38</sup> tunable filters,<sup>39</sup> optical isolators,<sup>40</sup> and programmable spatial light modulators,<sup>41</sup> have also been reported. This review paper, however, primarily covers research studies related to nonlinear optics.

Nonlinear optical processes have numerous applications in spectroscopy, quantum optics, and optical communication, among others. Since the first demonstration of second-harmonic generation (SHG) over six decades ago,<sup>42</sup> a vast variety of materials and platforms have been explored for nonlinear optics applications.<sup>43</sup> This review paper exclusively focuses on recent advancements in nonlinear integrated photonics on TFLN. Overviews of early developments of nonlinear effects in TFLN devices and recent progress on other materials can be found elsewhere.<sup>44–46</sup>

## 2 Second-Order Nonlinearity in Thin-Film Lithium Niobate

LN has been the primary material of choice for second-order nonlinear optics, owing to its large optical susceptibility ( $\chi^{(2)}$ ) with the largest coefficient of it being diagonal, relatively large refractive index ( $n_o = 2.21$  and  $n_e = 2.14$  at  $\lambda = 1550$  nm), low optical absorption, ultraviolet to mid-infrared optical transmission, and its ferroelectric property, which allows for efficient nonlinear processes through domain reversal. Several other materials have been traditionally considered for second-order nonlinear applications (e.g., see Table 1.5.3 in Ref. 43). For integrated solutions and in addition to LN, materials such as

**Table 1** Optical properties of some of the materials used for second-order nonlinear applications.

Material	Largest $d$ coefficient	Refractive index at 1550 nm
LiNbO <sub>3</sub> <sup>51</sup>	$d_{33} = 27$ pm/V	~2.2
AlN <sup>52</sup>	$d_{33} = 4.7$ pm/V	~2.1
GaAs <sup>51</sup>	$d_{36} = 119$ pm/V	~3.4
GaN <sup>53</sup>	$d_{33} = 16.5$ pm/V	~2.3

AlN,<sup>47</sup> (Al)GaAs,<sup>48,49</sup> and GaN,<sup>50</sup> have lent themselves to thin film on insulator waveguide platforms. Their nonlinear coefficients and refractive indices are listed in Table 1 and compared with LNs. GaAs has a very high  $d_{36}$  value but it is not a ferroelectric material, hence modal-phase matching (PM) is typically pursued, which, as argued later, is less favorable than quasi-PM among fundamental guided modes.

Initially, bulk material and conventional waveguides were used to explore the capabilities of LN for nonlinear applications.<sup>54–57</sup> Conventional waveguides, based on proton-exchange or titanium-diffusion, have demonstrated phenomenal performance and have been commercially available for several years.

Shortly after the emergence of TFLN on silicon substrates,<sup>4</sup> it was realized that this new platform could take the performance of nonlinear devices to a much higher level.<sup>13,58</sup> As shown in Fig. 1, owing to the compactness of TFLN waveguides provided by the high index contrast, optical mode sizes are remarkably smaller than those in conventional counterparts, hence much higher intensities can be achieved for the same optical power. Moreover, the overlap integral between the interacting optical modes at different wavelengths with the same parity is much larger. These differences result in significant improvements in efficiencies of various nonlinear processes. For example, the normalized conversion efficiency of second harmonic generation (SHG) has a direct relation to the overlap integral of the fundamental and second harmonic modes and an inverse relation to mode areas.<sup>46</sup> Moreover, bending radii in the TFLN platform are much smaller than in the conventional LN because of its high index contrast, hence efficient and ultracompact microresonator structures can be easily realized on this platform for integrated nonlinear applications.

Single-pass straight microwaveguides and resonant-based structures, such as microrings, microdisks, racetracks, and photonic crystals, have been used to investigate nonlinear integrated photonics on the TFLN platform. Classical second-order nonlinearities, such as SHG, sum-frequency generation (SFG), difference-frequency generation (DFG), optical parametric amplification (OPA), optical parametric oscillation (OPO), and the nonclassical spontaneous parametric downconversion (SPDC) process have been demonstrated, which are all covered in more details in the following sections.

It is well known that for an efficient nonlinear process, both the energy and momentum conservation conditions should be satisfied, the latter of which is not trivial due to waveguide and material dispersion. For example, SFG requires  $\omega_1 + \omega_2 = \omega_3$  and  $k_1 + k_2 = k_3$  or  $n_1\omega_1/c + n_2\omega_2/c = n_3\omega_3/c$ , where  $\omega_i$  denotes the angular frequencies of the participating signals in the nonlinear process, and  $k_i$  and  $n_i$  are the corresponding wavevector and refractive index, respectively.<sup>43</sup> For the case of SHG, in which  $\omega_1 = \omega_2$ ,  $k_1 = k_2$ , and  $n_1 = n_2$ , the energy and

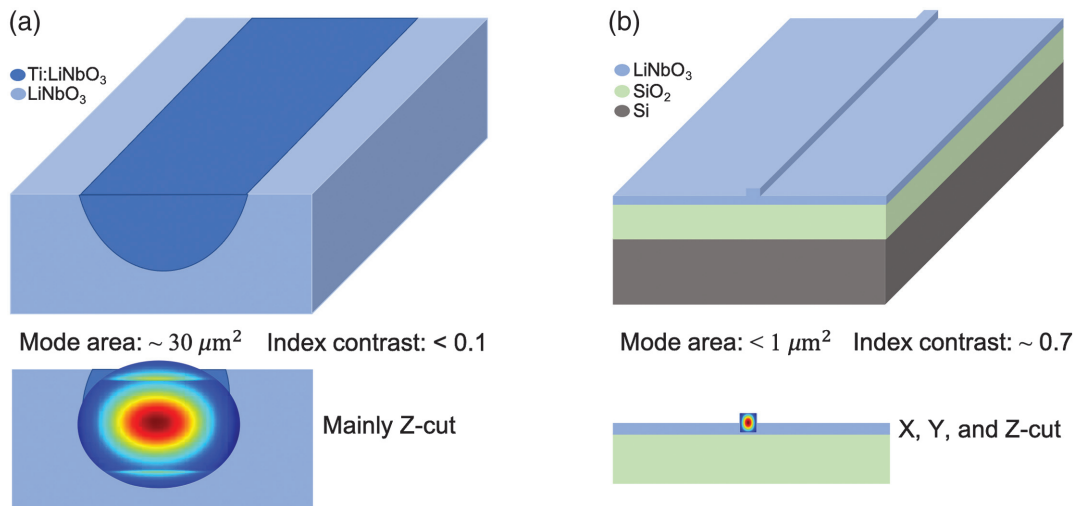


**Fig. 1** Comparison of optical mode areas, index contrast, and crystal orientations in (a) conventional LN waveguides and (b) thin-film LN waveguides.

momentum conservation conditions are simplified to  $\omega_3 = 2\omega_1$ ,  $k_3 = 2k_1$ , or  $n(\omega_1) = n(2\omega_1)$ . Similarly, these conditions should be fulfilled for other efficient nonlinear processes. In the presence of a wavevector mismatch (or as often referred to as phase mismatch), e.g.,  $\Delta k = k_1 + k_2 - k_3 \neq 0$  for SFG, the power oscillates between the participating frequencies instead of efficiently generating the targeted frequency. Therefore, PM becomes the most critical aspect of any nonlinear process. In addition, and in resonant-based structures, all the frequencies involved in an efficient nonlinear process should meet the resonance condition.

Various phase-matching methods are covered in Sec. 2.1 for SHG, which can be similarly applied to other three-wave mixing processes in TFLN. It is worth mentioning that for all these methods and considering the crystal orientation, the preferred polarization is, if possible, the one that utilizes the largest element in the  $\chi^{(2)}$  tensor of LN, i.e.,  $d_{33}$ . For instance, Fig. 2 shows the crystal orientation and preferred polarization for periodic poling and modal PM methods for straight waveguides. As shown in this figure, TFLN wafers are available in X-, Y-, and Z-cut orientations, and the desired polarization is chosen accordingly.

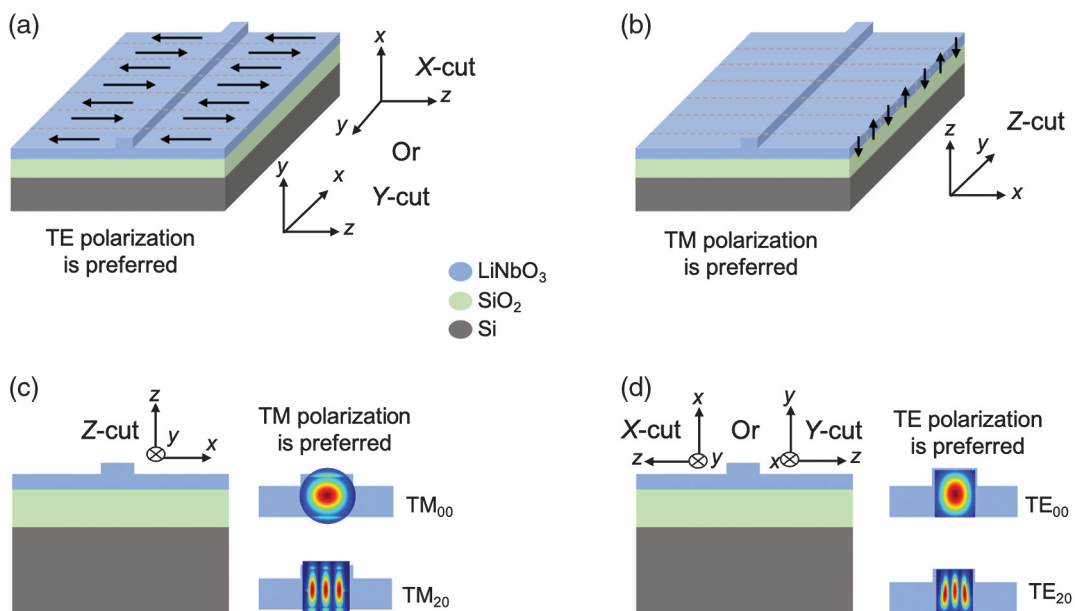


**Fig. 2** Crystal orientations and corresponding preferred polarization to achieve maximum efficiency for nonlinear processes in TFLN using [(a), (b)] quasi phase matching via periodic poling and [(c), (d)] modal phase matching.

### 2.1 Second-Harmonic Generation in TFLN

SHG is considered the most fundamental three-wave mixing process, and it is commonly used to evaluate the performance of new materials and platforms. Hence, it is not surprising that SHG accounts for a sizable portion of the published works on three-wave mixing in TFLN. SHG can be used in applications such as light generation at inconvenient wavelengths for conventional semiconductor light sources, ultrashort pulse width measurement, and second-harmonic microscopy. This section reviews influential SHG studies that use straight waveguides, as well as resonator-based with various phase-matching methods. It is noted that for SHG, when the polarizations of both the pump (fundamental) and the second harmonic (SH) waves are the same and along the extraordinary axis, the PM method is called type-0 PM; otherwise, it is called type-I PM.

Several phase-matching methods have been adopted or developed on TFLN (see Fig. 3). They can be divided into two broad categories.<sup>46</sup> The first group is perfect PM, which achieves  $\Delta k = 0$  by keeping the refractive indices for the fundamental and SH modes equal. Birefringent PM (BPM) and modal PM

(MPM) are two examples of perfect PM methods. Cyclic PM (CMP), which is used in microrings and microdisks, meets the  $\Delta k = 0$  condition for perfect PM in certain azimuthal angles. The second category is quasi-PM (QPM),  $\Delta k \neq 0$ , which is based on perturbing the nonlinear process to compensate for phase mismatches and includes grating-assisted QPM (GA-QPM) and periodic poling. Using metasurfaces, PM-free SHG is also possible.

The power relation of SHG in a lossless medium follows  $P_2 \propto (P_1 L)^2$ , where  $P_1$  and  $P_2$  are the pump and SH powers, respectively, and  $L$  is the device length.<sup>43</sup> Therefore, a normalized conversion efficiency is defined as  $\eta = P_2 / (P_1^2 L^2)$  with the unit of  $\% W^{-1} cm^{-2}$ . However, the proportionality to  $L^2$  is rarely held in practical waveguides, since the relation is only valid in the low-loss regime.<sup>46</sup> Therefore, it is worth considering the efficiency in units of  $\% W^{-1}$  as well for better performance evaluation and comparison. Such a normalized conversion efficiency, i.e.,  $P_2 / P_1^2$ , is typically reported for resonant-based structures. However, this again can lead to absurdly large numbers if  $P_1$  is very small, but without useful  $P_2$  values. It appears

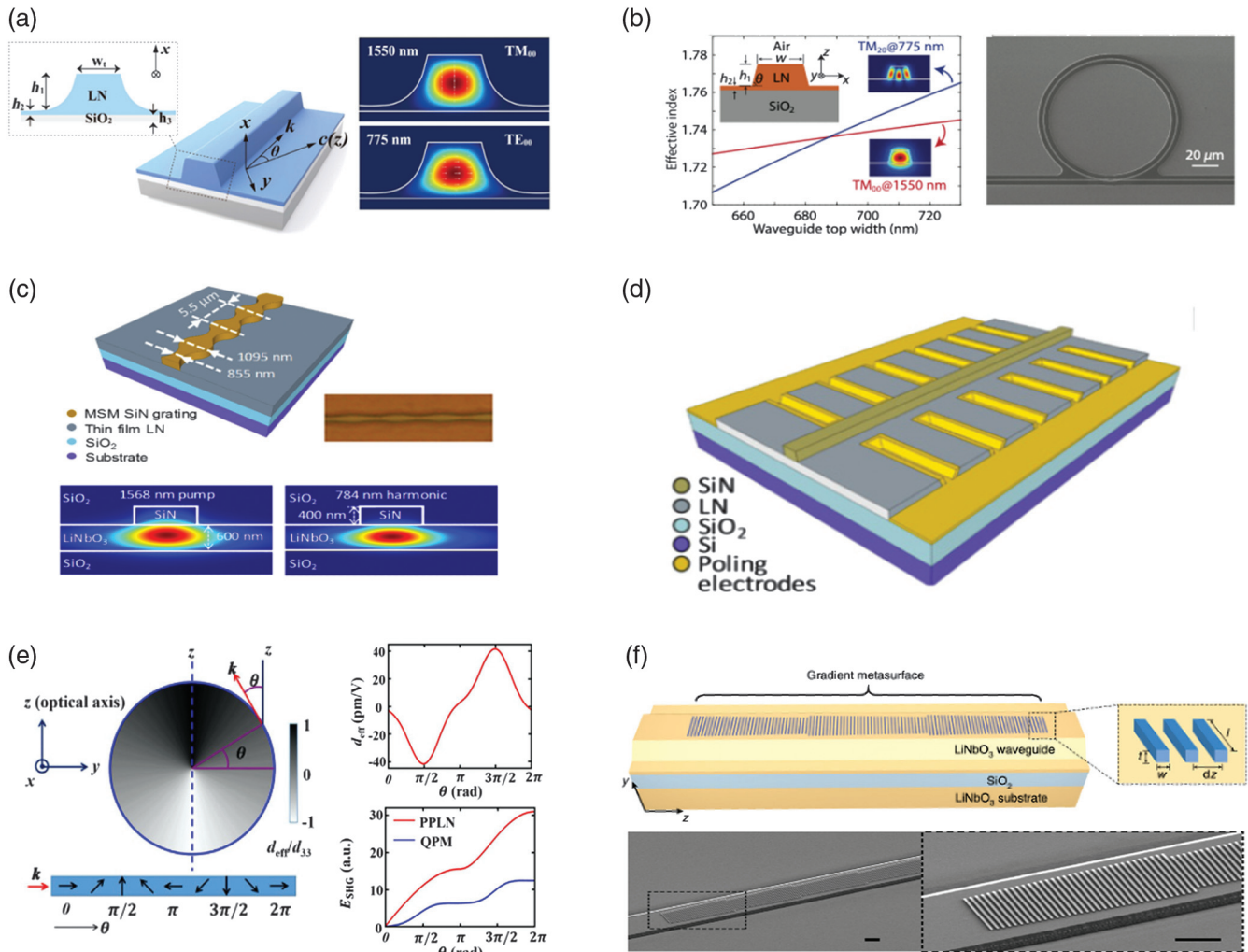


**Fig. 3** Various phase-matching methods used on the TFLN platform. (a) Birefringent phase-matching.<sup>59</sup> (b) Modal phase matching.<sup>60</sup> (c) Grating-assisted quasi phase matching or mode shape modulation.<sup>61</sup> (d) PPLN on a straight waveguide.<sup>13</sup> (e) Natural quasi phase matching, which is conceptually similar to cyclic phase-matching.<sup>62</sup> (f) Phase-matching-free metasurface.<sup>63</sup>

that the unitless absolute ratio of the output–input powers,  $P_2/P_1$  (expressed in %), may be the ultimate meaningful efficiency for most practical applications.

### 2.1.1 Birefringent phase matching

BPM can be attained in anisotropic materials by polarizing the fundamental and SH waves along different axes (type-I) to match the refractive indices at these frequencies and satisfy perfect PM. Although LN is a birefringent material, it is uncommon to use this method for SHG on TFLN, since it precludes the process from taking advantage of the largest element in the  $\chi^{(2)}$  tensor, corresponding to the nonlinear coefficient  $d_{33} = 27$  pm/V. This is in addition to the spatial walk-off issue and practical difficulties in implementing BPM, particularly in integrated chips. Nonetheless, Lu et al.<sup>59</sup> adopted an idea to demonstrate BPM on X-cut TFLN with an LN thickness of 10  $\mu\text{m}$ . The refractive index of the  $\text{TM}_{00}$  mode at the C-band fundamental wavelength was matched to that of the  $\text{TE}_{00}$  mode at the SH by deviating the 20-mm-long straight waveguide from the optical axis of LN by an angle of  $\theta = 52$  deg. Furthermore, the strong birefringence thermo-optic effect of LN was used to demonstrate a wide thermal tunability at a rate of 1.06 nm/K. The normalized conversion efficiency was, however, low ( $2.7\% \text{ W}^{-1} \text{ cm}^{-2}$ ). It seems that this design concept can be harnessed in other integrated birefringent materials, where QPM is not easily accessible.

### 2.1.2 Modal phase matching

In MPM, the dispersion of a multimode waveguide is engineered to accomplish equal effective refractive indices for the fundamental mode at the pump wavelength and a higher-order mode at the SH wavelength. Nonlinear devices based on MPM are easy to fabricate and are functional after forming the waveguide or the microring without the need for postprocessing steps, such as periodic poling. MPM has been employed for straight waveguides<sup>64,65</sup> and microresonator structures<sup>60,66</sup> in both type-0 and type-I configurations. The type-I implementation leverages the strong thermo-optic birefringence of LN and can tune the wavelength efficiently over a wide span at the expense of using the  $d_{31} = 4.7$  pm/V coefficient, which is more than five times smaller than  $d_{33}$ . However, even in the type-0 configuration, the SHG efficiency is limited due to using higher-order modes at the SH wavelength, which are less confined, have a higher propagation loss, and have a much weaker overlap integral with the fundamental mode at the pump wavelength. Luo et al.<sup>65</sup> demonstrated a type-I MPM in an 8-mm-long straight waveguide with a normalized SHG conversion efficiency of  $\eta = 7.3\% \text{ W}^{-1} \text{ cm}^{-2}$  and a tuning slope of 0.84 nm/K from 1560 to 1620 nm. Wang et al.<sup>64</sup> reported an  $\eta = 41\% \text{ W}^{-1} \text{ cm}^{-2}$  for a 1-mm-long device using type-0 MPM. Usually, the third-order mode is used at the SH wavelength, since the overlap integral between modes with different parities is equal to zero in a homogeneous waveguide. However, by adding complexity to the fabrication process and by having inhomogeneous waveguides consisting of  $\text{TiO}_2$  on LN, the  $\text{TE}_{00}$  mode for the pump and the  $\text{TE}_{01}$  mode for the SH were utilized with much stronger overlap integral, resulting in  $\eta = 650\% \text{ W}^{-1} \text{ cm}^{-2}$  in a 2.35-mm-long device.<sup>67</sup> Chen et al.<sup>66</sup> employed type-0 MPM and observed a 10-fold enhancement in SHG efficiency in a microring with 80  $\mu\text{m}$  radius compared with a 1-mm-long straight waveguide with the same cross-section. A relatively high conversion efficiency of  $1500\% \text{ W}^{-1}$

was demonstrated in a microring resonator with a 50  $\mu\text{m}$  radius using type-0 MPM.<sup>60</sup> MPM has been used in microdisk resonators as well, in type-0 configuration on a Z-cut TFLN.<sup>68–70</sup> However, the efficiencies in microdisks are much lower than microrings, and one of the best reported values for the normalized conversion efficiency appears to be  $\sim 11\% \text{ W}^{-1}$ .<sup>68</sup>

### 2.1.3 Grating-assisted quasi phase matching

In GA-QPM, also known as mode shape modulation,<sup>61</sup> guided modes are periodically perturbed to induce an extra phase term and compensate for the phase mismatch. Rao et al.<sup>61</sup> implemented a sinusoidal width variation in a TFLN waveguide rib-loaded with SiN, which resulted in an estimated  $\eta$  of  $\sim 1\% \text{ W}^{-1} \text{ cm}^{-2}$  for a 4.9-mm-long waveguide. Wang et al.<sup>64</sup> employed direct etching of TFLN to form periodically grooved waveguides with a groove depth of 80 nm and obtained  $\eta = 6.8\% \text{ W}^{-1} \text{ cm}^{-2}$  for a 500- $\mu\text{m}$ -long device.

### 2.1.4 Periodic poling in straight waveguides

Periodic poling, demonstrated first on bulk LN devices over a few decades ago,<sup>71</sup> is the most common and efficient QPM technique on LN, especially for straight waveguides, despite  $\Delta k \neq 0$ . In this method, to compensate for  $\Delta k$ , the sign of the relevant nonlinear coefficient is periodically altered in the areas that the power is supposed to be converted back to the pump frequency. A periodicity of  $\Lambda = 2\pi/\Delta k$  with a 50% duty cycle prevents power oscillation between interactive waves and facilitates a much more efficient power transfer from the pump to the targeted frequency. Devices made with this technique are called periodically poled lithium niobate (PPLN) and have been commercialized for many years. Poling is accomplished by utilizing the ferroelectric property of LN through domain inversion by applying electric fields greater than the coercive field. For congruent bulk LN, the coercive field value is  $\sim 21$  V/ $\mu\text{m}$ .<sup>72</sup> This value is higher in TFLN ( $\sim 40$  to 48 V/ $\mu\text{m}$ ), which is possibly related to the interface of  $\text{SiO}_2/\text{LN}$  bonding<sup>73</sup> or the annealing step of the wafer fabrication process and the subsequent out-diffusion of  $\text{Li}^+$  ions.<sup>74</sup> PPLN devices typically utilize  $d_{33}$  in a type-0 PM configuration in which the fundamental modes can be used for both the pump and SH wavelengths, resulting in a strong overlap integral and enhanced overall conversion efficiency. Extensive studies have been conducted to optimize the poling process parameters, e.g., preheat treatment, temporal waveform, and electric field strength for achieving a stable and uniform  $\sim 50\%$  duty cycle throughout the entire device.<sup>21–23,75</sup> Recently, several groups have successfully demonstrated submicron poling periods,<sup>76–78</sup> which are capable of compensating for large values of  $\Delta k$  and are of high demand, particularly for short-wavelength nonlinear devices and counter-propagating processes. Also, nondestructive measurement methods, such as piezo-response force microscopy (PFM), SH confocal microscopy,<sup>79</sup> and far-field diffraction,<sup>80</sup> are employed to visualize and evaluate the poling quality.

In 2016, PPLN devices were demonstrated for the first time on the TFLN platform on LN<sup>73</sup> and Si<sup>13</sup> substrates. Both devices relied on silicon nitride (SiN) rib-loaded waveguides on TFLN. Using SiN rib-loaded waveguides and by engineering the lateral leakage, a normalized conversion efficiency of  $1160\% \text{ W}^{-1} \text{ cm}^{-2}$  was achieved in 2019 for a 4.8-mm-long device.<sup>81</sup> Figure 4 shows various types of PPLN devices demonstrated in TFLN, such as straight waveguides and resonator structures.

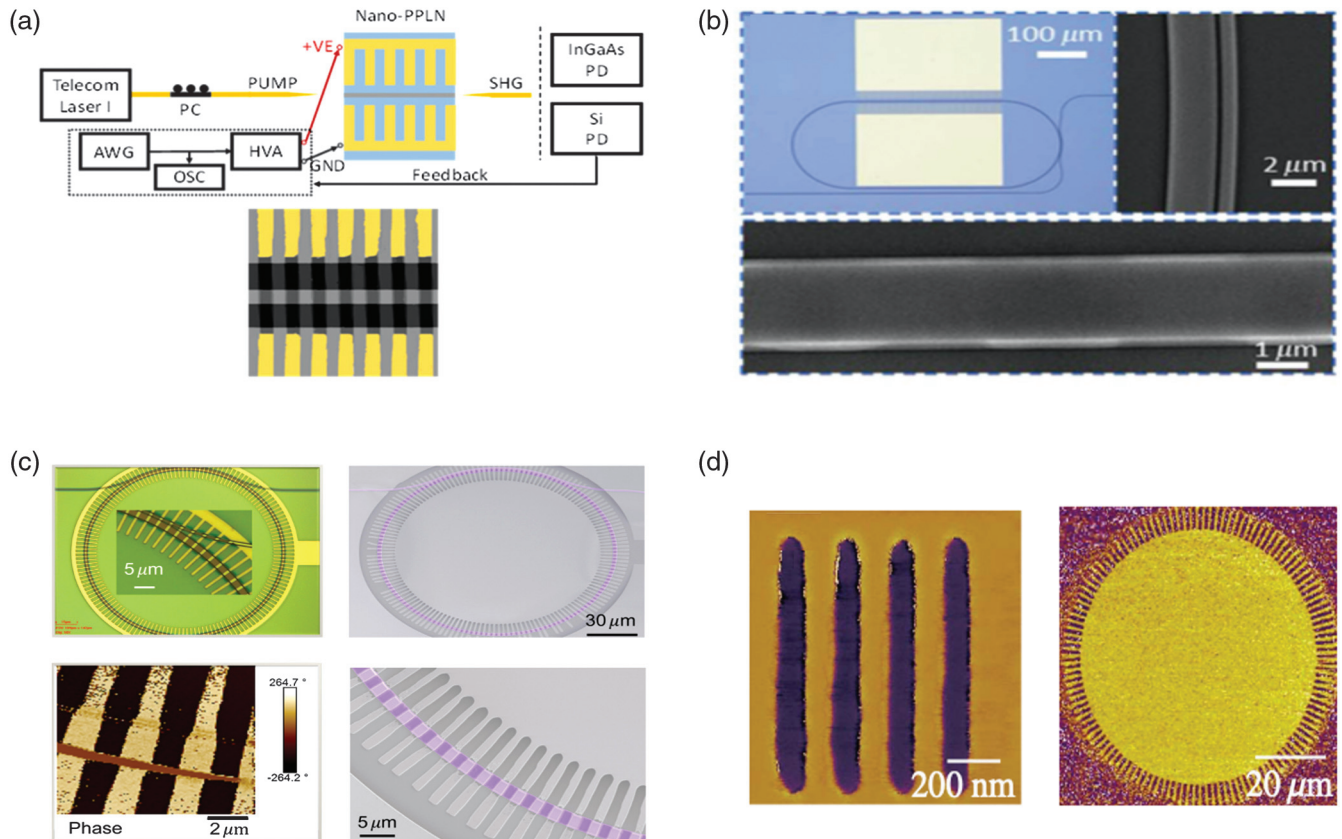


**Fig. 4** PPLN devices in different structures. (a) Straight waveguide.<sup>82</sup> (b) Racetrack resonator that is poled on one of the straight arms.<sup>83</sup> (c) Radially poled microring resonator.<sup>84</sup> (d) Radially poled microdisk, poled using the PFM technique in which they also demonstrated a poling period as small as 200 nm.<sup>85</sup>

Following the development of low loss etching processes,<sup>15</sup> ultrahigh efficient nonlinear processes on TFLN using direct etching emerged. In 2018, using direct etching on a MgO-doped X-cut TFLN, Wang et al.<sup>86</sup> reported normalized SHG conversion efficiencies of 2600 and 2300%  $W^{-1} cm^{-2}$  for 4-mm-long devices on two different waveguide widths operating at two distinct wavelengths. MgO-doping mitigates any potential photorefractive effects in LN, and hence enables high-power operation. Chen et al.<sup>87</sup> achieved a very similar performance on an undoped X-cut TFLN with an  $\eta$  of 2200%  $W^{-1} cm^{-2}$  for a 4-mm-long device. In 2019, our group showed a record high normalized SHG conversion efficiency to date of 4600%  $W^{-1} cm^{-2}$  on a 300- $\mu m$ -long device by actively monitoring the poling process and by performing multiple iterative cycles of poling and depoling.<sup>82</sup> In 2020, another very high  $\eta$  of 3757%  $W^{-1} cm^{-2}$  was reported on a longer device length of 5 mm.<sup>88</sup> Recently, a normalized conversion efficiency of  $\sim 320\% W^{-1} cm^{-2}$  was reported for a 20-mm-long device corresponding to  $\sim 1280\% W^{-1}$ ,<sup>89</sup> which is relatively high for conversion efficiencies reported to this date in units of %  $W^{-1}$  for straight waveguides (see Table 2).

### 2.1.5 Periodic poling in microresonators

Combining highly efficient PPLN devices with the intensified light-matter interaction in resonant-based structures has led to a new front in nonlinear processes. In 2019, Chen et al.<sup>83</sup> utilized a doubly resonant microcavity in a racetrack shape on

X-cut MgO-doped TFLN and periodically poled the 300- $\mu m$ -long straight waveguide on one arm to achieve a normalized conversion efficiency of 230,000%  $W^{-1}$  with only 5.6  $\mu W$  of pump power and a moderate  $Q$ -factor of  $3.7 \times 10^5$ . Lu et al.<sup>90</sup> radially poled a doubly resonant microring resonator on a Z-cut TFLN and were able to demonstrate  $\eta = 250,000\% W^{-1}$ . This is while they employed  $d_{31}$  by using  $TE_{00}$  for the pump mode and  $TM_{00}$  for the SH mode due to the difficulty of poling, since the poling period of type-0 PM would have been almost three times smaller. By utilizing  $d_{33}$  in the type-0 configuration through overcoming the poling issues and by improving the  $Q$ -factor of resonators, the same group reached 5,000,000%  $W^{-1}$  conversion efficiency at the low power regime with a pump power of  $\sim 10 \mu W$ .<sup>84</sup> As mentioned above, such very high efficiencies in %  $W^{-1}$  are possible because the ratio  $P_2/P_1^2$  would increase inversely with a decrease of the pump power for the same order of absolute power efficiency (see Table 3). Nonlinear optics at such low pump powers is a welcome development. However, as mentioned before, in most practical applications, the amount of the generated output power is more important and the absolute power efficiency,  $P_2/P_1$  in %, is therefore a more relevant figure of merit.

With a high single-photon coupling rate of 1.2 MHz and a reasonably low dissipation rate of 184.6 MHz, the previously cited work<sup>84</sup> reached a single-photon anharmonicity of 0.7%,<sup>84</sup> which could find application in integrated quantum photonics.<sup>92,93</sup> Periodically poled whispering-gallery resonators

**Table 2** Performance of various devices based on straight waveguide structure for SHG using different phase-matching methods. Power values for the pump and SH wavelength and the absolute conversion efficiency (in %) correspond to the maximum normalized conversion efficiency and are not necessarily the maximum reported numbers in these papers.

PM method	Pump/SH power	Length	% $W^{-1} cm^{-2}$	% $W^{-1}$	Absolute %
BPM type-I <sup>59</sup>	25 mW/67 $\mu W$	2 cm	2.7	10.7	~0.27
MPM type-0 <sup>67</sup>	630 $\mu W$ /140 nW	2.35 mm	650	36	~0.022
PPLN type-0 <sup>82</sup>	3 mW/370 nW	300 $\mu m$	4600	4.14	~0.012
PPLN type-0 <sup>88</sup>	530 $\mu W$ /2.7 $\mu W$	5 mm	3757	939.25	~0.5
PPLN type-0 <sup>86</sup>	1.5 mW/9.4 $\mu W$	4 mm	2600	416	~0.6
PPLN type-0 <sup>87</sup>	2.95 mW/31.6 $\mu W$	4 mm	2200	352	~1
PPLN type-0 <sup>89</sup>	~6 mW/550 $\mu W$	20 mm	~320	~1280	~9

**Table 3** Comparison of resonant-based structures for SHG using different phase-matching methods.

Structure	PM method	Pump/SH power	$Q_L$ at FW	% $W^{-1}$	Absolute %
Microring <sup>60</sup>	MPM type-0	440 $\mu W$ /2.9 $\mu W$	$1.4 \times 10^5$	1500	~0.65
Microring <sup>84</sup>	PPLN type-0	1.05 $\mu W$ /56 nW	$1.8 \times 10^6$	$5 \times 10^6$	~5.3
Microring <sup>90</sup>	PPLN type-I	55 $\mu W$ /7.5 $\mu W$	$8 \times 10^5$	$2.5 \times 10^5$	~13.5
Racetrack <sup>83</sup>	PPLN type-0	5.6 $\mu W$ /73 nW	$3.7 \times 10^5$	$2.3 \times 10^5$	~1.3
Microdisk <sup>91</sup>	CPM type-I	10 mW/110 $\mu W$	$1.1 \times 10^5$	~110	~1.1
Microdisk <sup>16</sup>	NQPM type-0	30 $\mu W$ /4.2 $\mu W$	$7.5 \times 10^7$	$4.7 \times 10^5$	~14

and microdisks are also demonstrated,<sup>85,94,95</sup> but with much lower conversion efficiencies. Nonetheless, the developed poling techniques for microdisks using PFM are invaluable and pave the way for reaching poling periods below 100 nm<sup>95</sup> [see Fig. 4(d)].

### 2.1.6 Cyclic phase matching

The CPM method<sup>96</sup> is used in microresonators on X- and Y-cut TFLN in a type-I configuration.<sup>91,97,98</sup> Since the ordinary refractive index of LN is larger than the extraordinary value, the pump signal is polarized perpendicularly to the optical axis and hence holds a constant ordinary refractive index while the SH wave is in-plane and experiences an oscillating refractive index between the ordinary and extraordinary indices as it rotates around the resonator structure. Accordingly, the PM condition is met at four different azimuthal angles at each round. The normalized conversion efficiency for the CPM method has a record of only 110%  $W^{-1}$ .<sup>91</sup> However, it benefits from wider PM bandwidths<sup>97</sup> and does not require periodic poling.

In 2019, a method very similar to CPM, but in type-0 configurations, was demonstrated and was called natural QPM.<sup>62</sup> Herein, the in-plane waves on X- or Y-cut TFLN undergo different effective nonlinear coefficients as they rotate around the resonator structure, which resembles the domain inversion and QPM without periodic poling. Using this method, a broad PM bandwidth with a normalized conversion efficiency of 9900%  $W^{-1}$  was reported.<sup>62</sup> Recently and partially due to a record high intrinsic  $Q$  of above  $10^8$ , natural QPM with a conversion efficiency of 470,000%  $W^{-1}$  was achieved in an ultra-broadband nonlinear device.<sup>16</sup> Also, an absolute conversion

efficiency of 23% was reported at a saturation pump power of 110  $\mu W$ .

### 2.1.7 Metasurfaces and photonic crystals

Phase-matching-free SHG is also possible using metasurface structures, which usually can operate over a wide range of wavelengths. This has been done, for example, by utilizing Mie-type resonant structures,<sup>63,99,100</sup> optical anapole modes,<sup>101</sup> and resonant waveguide gratings.<sup>102,103</sup> Among these, one of the best performances so far ( $\eta_{\max} = 1660\% W^{-1} cm^{-2}$ ) belongs to phased-array antennas forming a gradient metasurface, which provides a unidirectional wavevector and deprives the SH of converting back to the pump wavelength. A more detailed review on SHG using metasurface structures can be found elsewhere.<sup>104</sup>

Also, photonic crystals can be potentially very efficient in nonlinear processes due to their extremely small mode sizes and a strong light-matter interaction.<sup>105,106</sup> However, they require an elaborate doubly resonant design to overcome their typical low  $Q$ -factors and external coupling at SH, which remains a challenging task.

### 2.1.8 Summary and concluding remarks on SHG

Tables 2 and 3 summarize the performance of various devices for SHG using different phase-matching methods for straight waveguides and resonant-based structures, respectively. In these tables, maximum normalized conversion efficiencies along with the corresponding on-chip optical power at the fundamental and SH wavelengths and the absolute conversion efficiency are reported. The power values are mostly extracted from the related

plots in these published works. It is noted that some of these studies reported higher absolute conversion efficiencies at the high-power regime, where SH and pump powers do not follow the quadratic relation anymore and hence the normalized conversion efficiency is lower. In straight waveguides, PPLN devices have demonstrated the best performance in all conversion efficiency units. In resonant-based structures, again PPLN devices have exhibited a superior performance. However, the best absolute conversion efficiency belongs to a microdisk working with the natural QPM method,<sup>16</sup> which originates from the record-high loaded  $Q$ -factor of this resonator that is almost two orders of magnitude higher than the PPLN-based counterparts.

Comparing the two tables shows that conversion efficiencies reported in units of  $\% W^{-1}$  are mostly orders of magnitude larger for resonant-based structures. This notable difference is arising from the fact that straight waveguides are usually pumped at milliwatt levels, while resonant-based structures often work at microwatt levels. The absolute conversion efficiency is also higher in resonant-based structures. However, straight waveguides can handle very high powers, which can result in large absolute conversion efficiency values. For instance, an absolute conversion efficiency of 53% has been reported with 117 mW at SH when it was pumped with 220 mW in a MgO-doped TFLN waveguide.<sup>86</sup> Generation of SH at such high power levels is desired for many applications. Moreover, from the practical perspective, straight waveguides are generally less sensitive to thermal, vibrational, and other environmental fluctuations and have higher fabrication yield compared with resonant-based structures, which are very sensitive to fabrication errors. Finally, most of the high-performance resonant structures were pumped with TM polarized light on a Z-cut TFLN to utilize  $d_{33}$ , which can be a limiting factor for an ultimate integrated photonic chip, since semiconductor quantum-well lasers typically emit TE-polarized light and hence a polarization rotator is required for TM pumping.

## 2.2 Other Three-Wave Mixing Processes in TFLN

Other second-order nonlinearities, such as SFG, DFG, optical parametric oscillation/amplification (OPO/OPA), and SPDC, have been demonstrated on TFLN. Moreover, various three-wave mixing processes have been cascaded on this platform and resulted in outstanding performances for processes such as low (third and fourth) harmonic generation. All these processes will be briefly reviewed in the following sections.

### 2.2.1 Sum-frequency generation

The SFG process is very similar to SHG, in principle, with the ability to mix two distinct wavelengths, which makes it suitable for numerous applications. SFG can be used to generate light at frequency ranges where SHG cannot be utilized due to the lack of efficient lasers. It is also very common to use SFG for upconversion detection. For instance, low-power mid-infrared (mid-IR) light, down to a single-photon,<sup>107</sup> can be converted to visible wavelengths and detected using low-noise and high-performance visible detectors. SFG on TFLN has been demonstrated on both straight waveguides<sup>82,108</sup> and resonant-based structures.<sup>105,109,110</sup>

Our team demonstrated an SFG bandwidth of  $\sim 20$  nm in a TFLN PPLN device with a normalized conversion efficiency of  $\sim 900\% W^{-1} cm^{-2}$  when one of the lasers was at a fixed wavelength and the other one was swept within its tuning range.<sup>82</sup>

In addition, swiping both lasers resulted in an SFG from 1460 to 1620 nm. In microdisk resonators, a conversion efficiency of  $2.2 \times 10^{-3} W^{-1}$  is reported with a relatively low  $Q$  of  $1.8 \times 10^5$  using the MPM method.<sup>110</sup> Ideally, the conversion efficiencies four times larger than SHG should be achieved for SFG.<sup>111</sup> Therefore, having state-of-the-art values for  $Q$  and utilizing natural QPM or PPLN—as the most efficient PM methods for resonators so far—can notably boost the efficiency of SFG.

SFG can be combined with other second-order nonlinear phenomena, such as SHG, to obtain highly efficient higher-order nonlinear processes through cascading,<sup>62,69,112–115</sup> which will be discussed later in a separate subsection. Moreover, SFG has been cascaded with the EO effect, which is in principle a second-order nonlinear process as well. This is very useful for low-power and high-speed control of an SFG.<sup>116</sup>

### 2.2.2 Difference-frequency generation and parametric amplification and oscillation

DFG, OPA, and OPO share similar working principles. DFG has been extensively used for generating terahertz and mid-IR sources on other platforms.<sup>117,118</sup> On the TFLN platform, DFG has been demonstrated using both straight waveguides<sup>40,119</sup> and resonant-based structures.<sup>60</sup> A new hybrid TFLN/Si platform is proposed by providing numerical simulation results to utilize DFG for terahertz generation,<sup>120</sup> though it appears to be challenging to be realized from the fabrication perspective. Using periodically poled TFLN on sapphire—with a transparency window up to  $4.5 \mu m$ —mid-infrared generation up to  $3.66 \mu m$  with a DFG normalized conversion efficiency of  $200\% W^{-1} cm^{-2}$  is demonstrated.<sup>119</sup> Sapphire helps with circumventing the high absorption loss of the oxide layer at wavelengths longer than  $2.5 \mu m$ .<sup>58,119</sup> Cascaded SHG/DFG is used to demonstrate effective four-wave mixing on a microdisk on TFLN using MPM.<sup>70</sup> In collaboration with Johns Hopkins University, we have utilized DFG in a TFLN PPLN device and spectral filtering to demonstrate an optical isolator concept based on nonlinear optics.<sup>40</sup> The isolator has a wide bandwidth ( $>150$  nm) with 40 dB transmittance difference between forward and backward-propagating waves.

OPAs have been recently pursued on TFLN.<sup>121,122</sup> On-chip amplification, combined with phenomenal properties of LN, opens the door wide open for applications in sensing, communications, and quantum information processing, among others. Recently, using dispersion engineered PPLN devices, Ledezma et al.<sup>123</sup> reported on a phase-sensitive gain of 11.4 dB on a 2.5-mm-long device ( $\sim 45$  dB/cm) with a pump pulse energy of 0.8 pJ. They also demonstrated optical parametric generation with a 110 dB/cm gain with  $<6$  pJ of pump pulse energy and more than 600 nm gain bandwidth. Jankowski et al.<sup>124</sup> circumvented the group-velocity dispersion and temporal walk-off effects via delicate dispersion engineering in a TFLN PPLN device and reported on a 118 dB/cm of unsaturated parametric gain over  $1 \mu m$  of bandwidth with 4 pJ pulse energies. They also achieved a saturated gain of 146 dB/cm and a conversion efficiency of 15% for pulse energies above 10 pJ. These gain values are comparable with the state-of-the-art semiconductor optical amplifiers but with a much higher bandwidth that can potentially initiate numerous applications for TFLN.

OPOs can be utilized as a classical source for the generation of coherent radiations throughout a wide range of frequencies or as a nonclassical source for purposes such as quantum random number generation. Ultralow threshold ( $30 \mu W$ ) integrated OPO

devices are recently reported on the TFLN platform using a radially poled PPLN microring.<sup>125</sup> This OPO is widely tunable through varying the temperature and the pump wavelength and showed an 11% conversion efficiency at a pump power of 93  $\mu\text{W}$ .

### 2.2.3 Spontaneous parametric downconversion

SPDC is a nonclassical three-wave mixing process in which a pump photon generates two entangled photons, i.e., signal and idler, at lower frequencies.<sup>126</sup> For over three decades, SPDC has been used as a source in various quantum mechanical experiments, such as quantum cryptography<sup>127</sup> and quantum teleportation,<sup>128</sup> and it is usually more efficient than the third-order counterpart of spontaneous four-wave mixing.

TFLN is a propitious candidate for integrated quantum photonics. SPDC has been demonstrated on straight PPLN waveguides,<sup>87,129–133</sup> as well as on resonant-based structures.<sup>97,134</sup> In collaboration with Northwestern University, our team has reported quantum-correlated photon pairs with a high coincidence-to-accidental ratio (CAR) of beyond  $10^3$  over 140 nm<sup>129</sup> (on the same discussed PPLN devices with 300  $\mu\text{m}$  lengths that exhibited an SHG efficiency of 4600%  $\text{W}^{-1}\text{cm}^{-2}$ ).<sup>82</sup> In another publication, we demonstrated correlated photon pairs using cascaded SHG and SPDC in a single 4-mm-long PPLN device.<sup>130</sup> A comprehensive review of integrated quantum photonics on the TFLN platform can be found elsewhere.<sup>135</sup>

Over the past two years, several high-performance SPDC devices based on PPLN structures are demonstrated. Zhao et al.<sup>132</sup> reported a CAR of  $\sim 67,000$  at a pair flux of 76 kHz and a CAR of  $\sim 670$  at a pair flux of 11.4 MHz for a 5-mm-long PPLN waveguide. A spectral brightness of  $5.6 \times 10^7 \text{ Hz nm}^{-1} \text{ mW}^{-1}$ , visibility of  $>99\%$ , and heralded single-photon autocorrelation of  $g_H^{(2)}(0) < 0.025$  were measured for this device as well. Xue et al.<sup>131</sup> showed an ultrahigh pair flux rate and a spectral brightness of  $2.79 \times 10^{11} \text{ Hz mW}^{-1}$  and  $1.53 \times 10^9 \text{ Hz nm}^{-1} \text{ mW}^{-1}$ , respectively, on a 6-mm-long PPLN waveguide at the expense of a lower CAR value of about 600. This device possessed 160 nm of bandwidth and maximum visibility of  $\sim 99\%$ . Recently, Javid et al.<sup>133</sup> demonstrated a record high bandwidth of 800 nm (100 THz) in a 5-mm-long dispersion engineered PPLN waveguide. A CAR of  $>150,000$  at a pair flux of 176 kHz, a spectral brightness of  $3.8 \times 10^7 \text{ Hz nm}^{-1} \text{ mW}^{-1}$ , and a visibility of 98.8% were reported for this device. Using a radially poled microring resonator on the TFLN platform, Ma et al.<sup>134</sup> demonstrated pair fluxes of 36.3 and 8.5 MHz at pump powers as low as 13.4 and 3.4  $\mu\text{W}$ , respectively. Also, a maximal CAR of  $\sim 15,000$  and a minimal  $g_H^{(2)}(0)$  of 0.008 were reported for this PPLN microring. These devices have already met or in some cases surpassed the performance of other materials, such as Si, SiN, AlN, and bulk LN. Therefore, a bright future is expected for quantum integrated photonics on TFLN.

### 2.2.4 Cascading second-order nonlinear processes

Higher-order harmonics and wave mixing effects can occur by cascading  $\chi^{(2)}$  processes in a single or multiple TFLN devices. Furthermore, effective third-order nonlinearities can be realized through cascading  $\chi^{(2)}$  processes.<sup>136</sup> This is specifically very intriguing for the TFLN platform since  $\chi^{(2)}$  of LN is much stronger than its other nonlinearities. Cascading  $\chi^{(2)}$  processes has been extensively studied on the TFLN platform to further improve the performance of other nonlinear processes.<sup>69,70,89,114,115,130,137–139</sup>

There are several methods to achieve such cascading effects (see Fig. 5). A straightforward method is by placing two or more different periodically poled sections, each being responsible for a specific  $\chi^{(2)}$  process. For instance, our group demonstrated two devices (each with two cascaded PPLN sections) for low-harmonic generation, namely third- and fourth- harmonic generations (THG and FHG). For THG, the first PPLN segment was designed for SHG while the second PPLN was responsible for SFG, resulting in a cascaded SHG/SFG ( $\omega + \omega \rightarrow 2\omega/2\omega + \omega \rightarrow 3\omega$ ). For FHG, both PPLN segments were poled for SHG, resulting in SHG/SHG ( $\omega + \omega \rightarrow 2\omega/2\omega + 2\omega \rightarrow 4\omega$ ).<sup>137</sup> Another method is to have more than one period in a PPLN device and generate a wider range of  $k$ -vectors to compensate for different phase-mismatching required for various nonlinear processes. This has been done in a chirped PPLN straight waveguide, which resulted in illustration of high-harmonics up to the 13th harmonic.<sup>115</sup> Also, a PPLN microdisk with a dual period was utilized for THG and FHG.<sup>95</sup> In addition, it is possible to achieve cascading in a single PPLN waveguide for THG and FHG via pulse pumping and by slightly detuning the pump wavelength from the QPM wavelength.<sup>82,89,139</sup> This latter method was used to demonstrate self-phase modulation with an effective nonlinear refractive index, i.e.  $n_{2,\text{eff}}$ , that is almost 200 times larger than the intrinsic  $n_2$  of LN in a dispersion-engineered PPLN waveguide.<sup>139</sup> The effective  $\chi_{\text{eff}}^{(3)}$  reported in this paper is larger than that of other well-known photonic Kerr-based platforms (such as Si and SiN) and proves the effectiveness of the cascading process. Moreover, in the first reported cascaded  $\chi^{(2)}$  for THG in a resonator, it was shown that natural BPM can be employed to observe both SHG and THG at higher values of pump power.<sup>69</sup>

## 2.3 Applications of Second-Order Nonlinearity in Optical Frequency Combs

An optical frequency comb (OFC) consists of a large number of equidistant teeth in the optical spectra with potential applications in accurate optical clocks, optical communication, detection and ranging, spectroscopy, and sensing.<sup>140</sup> TFLN in particular is a very attractive platform for OFCs since dispersion engineering is fairly easy on this platform, and it enables OFC generation through different processes, such as  $\chi^{(3)}$ , cascaded  $\chi^{(2)}$ , and the EO effect. Moreover, TFLN can leverage other phenomenal properties of LN to provide additional devices, such as self-referencing components, EO modulators, frequency converters, and filters to materialize a fully functional integrated chip for OFC generation.

The most common method for OFC generation is based on the Kerr effect, which is a third-order nonlinear process and will be discussed in Sec. 3.2. In another approach, OFC generation through only  $\chi^{(2)}$  processes is also possible and is called quadratic frequency combs. This can be done through an OPO cascaded with SHG/SFG or the other way around. In other words, quadratic frequency combs leverage LN's large second-order nonlinear coefficients and can result in a lower threshold and higher efficiency compared with Kerr combs. Moreover, the frequency shifting nature of this process makes it possible to generate OFCs at the mid-IR or ultraviolet wavelengths using the commonly available visible and near-IR lasers. On-chip integration of  $f - 2f$  self-referencing is feasible as well. However, such combs have been mostly demonstrated on table-top systems.<sup>141</sup> Recently, an on-chip quadratic frequency comb with

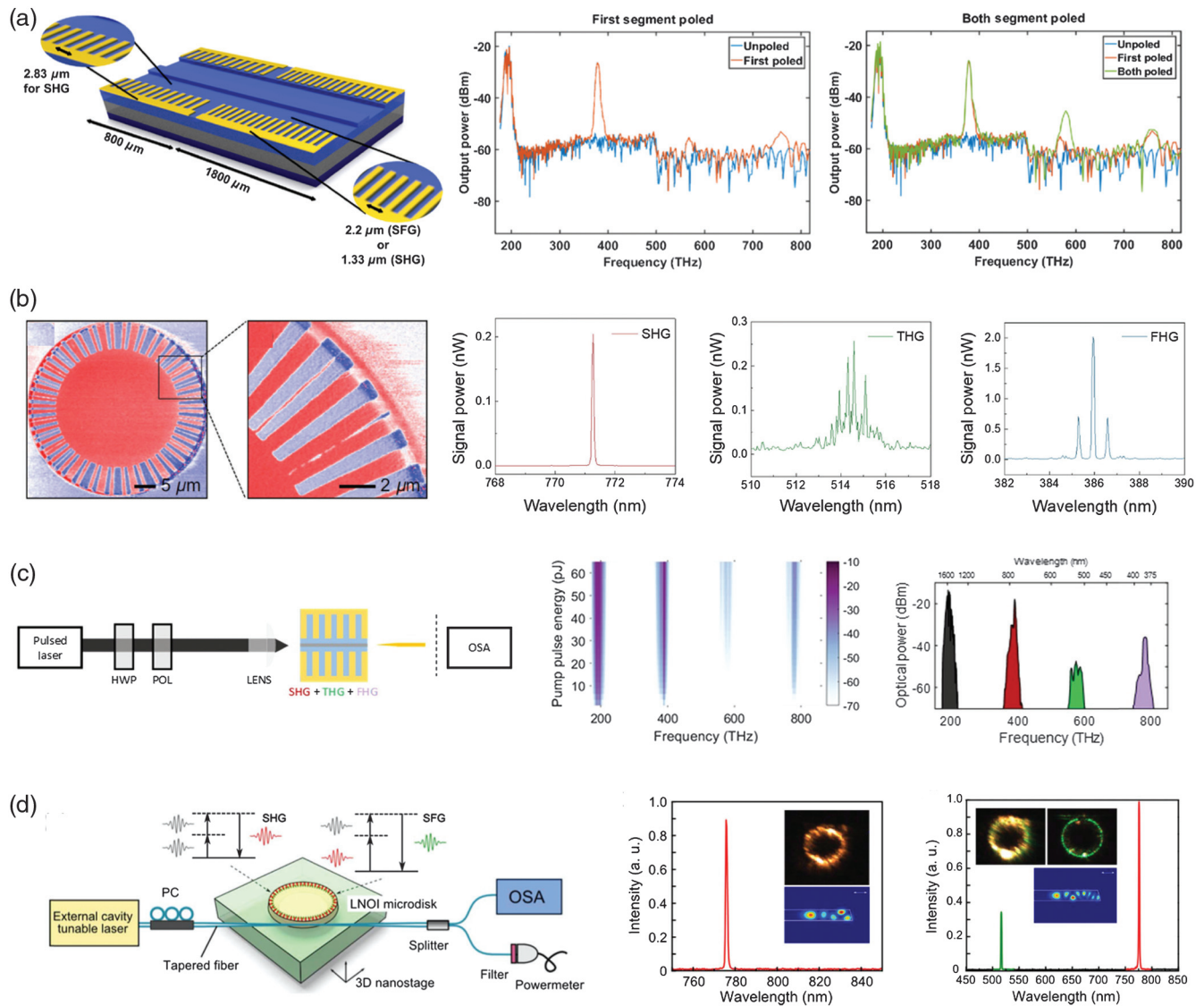


**Fig. 5** Some of the schemes used for implementing cascaded  $\chi^{(2)}$  processes in TFLN and the corresponding harmonic generations. (a) Two PPLN sections with different poling periods to enable SHG/SFG cascading for a THG device and SHG/SFG for an FHG device.<sup>137</sup> (b) Dual-period PPLN microdisk with demonstrated THG and FHG.<sup>95</sup> (c) THG and FHG on a single PPLN device via pulse pumping.<sup>82</sup> (d) SHG and THG on a microdisk through cascaded SHG/SFG by taking advantage of the natural BPM.<sup>69</sup>

a soliton state was illustrated in an AlN platform.<sup>142</sup> Quadratic OFCs, operating in the modulation instability regime, have been reported on conventional LN chips using PPLN waveguides and a microresonator<sup>143–147</sup> [Fig. 6(a)]. This type of OFC has yet to be demonstrated on the TFLN platform.

EO combs are another alternative for OFC generation. Although EO is fundamentally a  $\chi^{(2)}$  nonlinear process, the EO combs are not regarded as a variant of the quadratic frequency combs discussed above, since their working principle is different. In the EO scheme, comb lines are formed by generating sidebands of the pump signal through phase modulation.<sup>149</sup> To increase the number of lines, usually a resonator structure such as a Fabry–Pérot cavity<sup>150</sup> or a microresonator<sup>151</sup> is used in which the frequency of the applied RF signal matches an integer number of the resonator’s free-spectral range. The line

spacings of these OFCs are tunable, and the spectral flatness compared with Kerr combs can be achieved on them by proper designs. However, due to the small frequency spacing compared with Kerr combs, EO combs have limited bandwidths. A review on the advancement of integrated EO combs on different platforms can be found elsewhere.<sup>152</sup>

On the TFLN platform and by proper dispersion engineering in a microresonator structure with  $Q \approx 1.5 \times 10^6$ , Zhang et al.<sup>151</sup> were able to expand the spectral span of an EO comb to 80 nm with a spectral slope of  $\sim 1$  dB/nm and a pump to comb conversion efficiency of  $\sim 0.3\%$ . The spectra comprised more than 900 comb lines with a repetition rate of  $\sim 10.45$  GHz. Recently, the same group used two coupled resonators that were critically coupled when applying the RF modulation signal and hence transferred the pump power much more efficiently

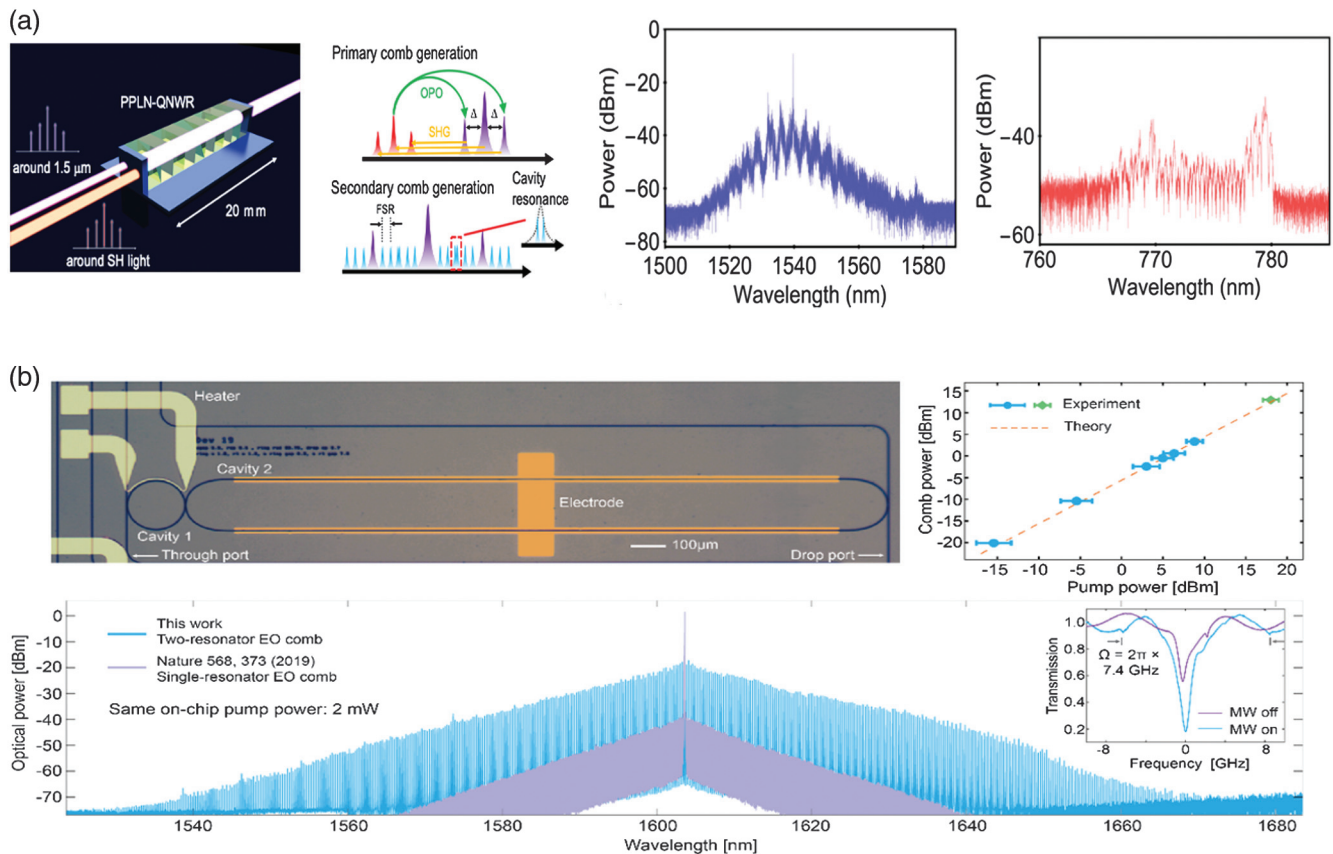


**Fig. 6** Using second-order nonlinear processes for generating OFCs on lithium niobate. (a) Quadratic frequency comb generation on conventional LN<sup>143</sup> using cascaded  $\chi^{(2)}$  processes, which has yet to be demonstrated on the TFLN platform. (b) Electro-optic frequency comb generation in TFLN using coupled microring and racetrack resonators and the resulting spectrum exhibiting a high conversion efficiency.<sup>148</sup>

into the microresonator.<sup>148</sup> This new configuration resulted in conversion efficiency of 30% with a spectral span of 132 nm and a comb line spacing of  $\sim 31$  GHz [Fig. 6(b)]. In addition, it was shown that this EO comb, with such bandwidth and conversion efficiency, can be used as a high peak power ultrafast pulse source ( $\sim 336$  fs pulse duration) for other on-chip nonlinear processes including Kerr comb generation.

### 3 Third-Order Nonlinear Processes in TFLN

Although the third-order nonlinear coefficient of LN ( $1.6 \times 10^{-21}$  m<sup>2</sup>/V<sup>2</sup>) is not as exceptionally high as its second-order coefficient compared with other materials, it is still very large and comparable to SiN, which is a popular choice for third-order nonlinear applications. Utilizing LN  $\chi^{(3)}$  coefficients, combined with the recently achieved ultralow propagation loss and compact mode sizes of TFLN, makes the platform appealing for high-performance third-order nonlinear devices.

Among several well-known third-order nonlinear interactions, e.g., four-wave mixing,<sup>153</sup> stimulated Brillouin scattering,<sup>154</sup> and Raman processes,<sup>155</sup> some have been demonstrated on the TFLN platform.<sup>30,156</sup> However, due to the limited space, this work only covers supercontinuum generation (SCG) and Kerr effect in resonant structures, with an emphasis on their applications in OFCs.

#### 3.1 Supercontinuum Generation

SCG is a nonlinear process where an ultrashort pulse with enough intensity experiences spectral broadening after propagating a certain distance through a third-order nonlinear medium.<sup>140</sup> SCG typically requires anomalous group velocity dispersion (GVD). However, it can be also achieved in the marginally normal GVD regime at the expense of higher pulse powers.<sup>157</sup> Spectral broadening of more than one octave is particularly useful for OFCs, since the wide spectrum allows stabilization of the carrier-envelope offset (CEO) frequency,  $f_{\text{CEO}}$ , through the  $f - 2f$  self-referencing method. SCG on integrated platforms benefits from ease of dispersion engineering and compact waveguide sizes and hence operates at lower energies. TFLN is a great platform for SCG as it offers a strong  $\chi^{(2)}$  nonlinearity in addition to the required  $\chi^{(3)}$ , hence enables on-chip  $f - 2f$  self-referencing<sup>158</sup> [Fig. 7(c)].

Lu et al.<sup>160</sup> demonstrated SCG with 1.5 octaves of bandwidth using 800 pJ of pulse energy in a 10-mm-long Z-cut TFLN waveguide. In another work, 2.58 octaves of bandwidth using a pulse energy of 185 pJ was achieved in a 5-mm-long waveguide on an X-cut TFLN<sup>159</sup> [Fig. 7(a)]. In addition to SCG, SHG and SFG were observed in this study, which were attributed to MPM at higher-order spatial modes. With the SCG spectrum overlapping with that of SHG, the  $f_{\text{CEO}}$  beat-note was directly detected with a 30-dB signal-to-noise ratio (SNR). Jankowski

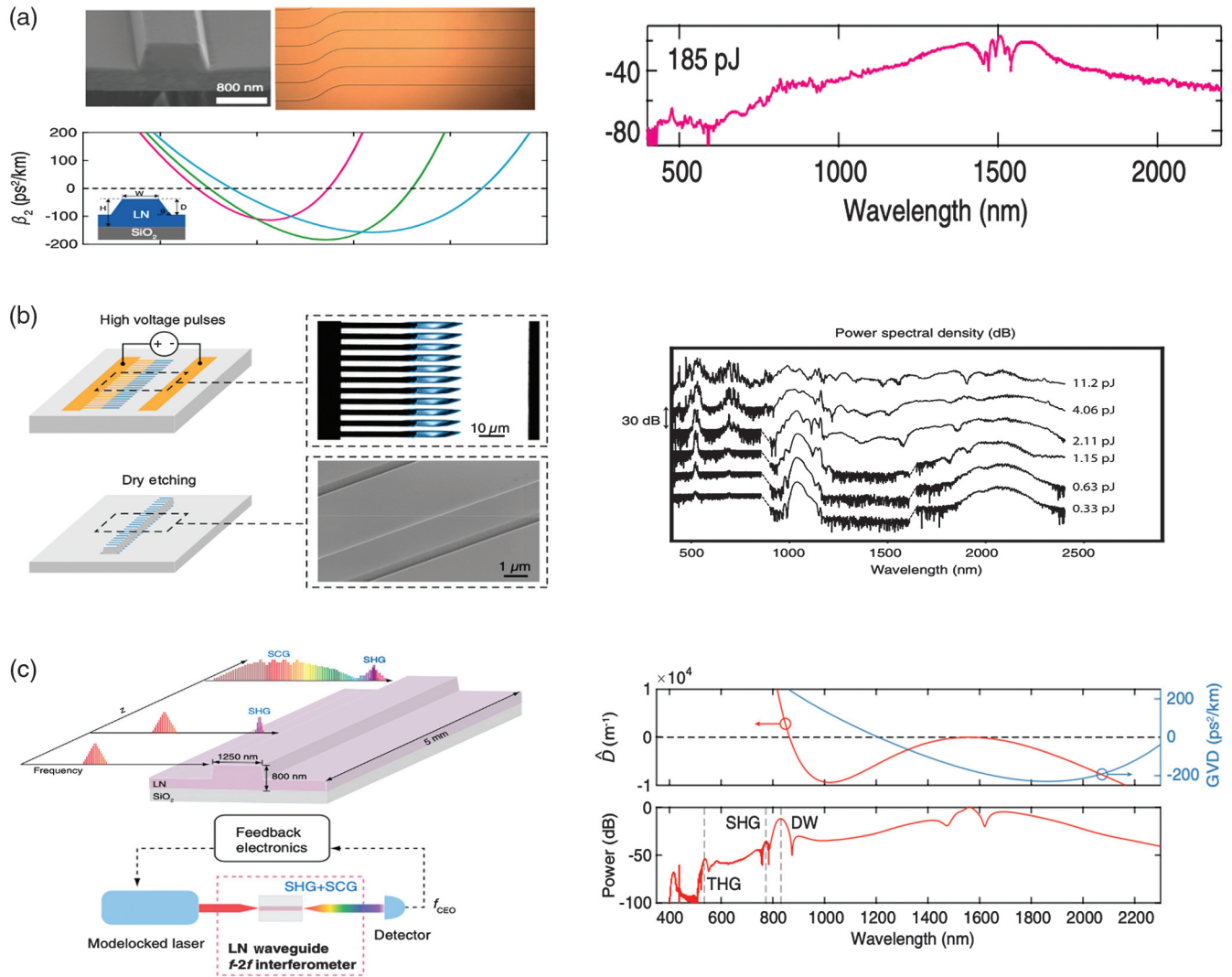


**Fig. 7** SCG on the TFLN platform. (a) SCG spanning over two octaves in a dispersion engineered straight waveguide without poling.<sup>159</sup> (b) SCG on a periodically poled straight waveguide with a span of more than two octaves at a pulse energy of  $\sim 11$  pJ.<sup>139</sup> (c) Using cascaded SCG and SHG for on-chip  $f-2f$  self-referencing, which is of great importance for realization of on-chip OFCs.<sup>158</sup>

et al.<sup>139</sup> used a 6-mm-long PPLN waveguide to take advantage of cascaded  $\chi^{(2)}$  processes and achieved more than two orders of magnitude improvement in self-phase modulation compared with that of Kerr nonlinearities. This resulted in an SCG with  $>2.5$  octaves span at only  $\sim 11$  pJ of pulse energy. To confirm the coherency of the SCG, they measured the  $f_{\text{CEO}}$  beat-note with an SNR of 35 dB.

### 3.2 Kerr Effect in Microresonators for Optical Frequency Comb Generation

Soliton OFCs can be generated over a wide bandwidth in microresonator structures with anomalous dispersion and by relying on the Kerr ( $\chi^{(3)}$ ) nonlinearity. Using these combs, as the conceptual schematic in Fig. 8(a) suggests, versatile properties of TFLN can be utilized for the realization of fully integrated soliton combs on a single chip with providing all the necessary components.<sup>161</sup> He et al.<sup>161</sup> demonstrated soliton microcombs with a comb teeth spacing of  $\sim 200$  GHz over a  $>200$  nm

spanning range around  $\lambda = 1550$  nm in a Z-cut microring resonator with a  $Q$  of  $2.2 \times 10^6$ . They also showed that the photorefractive effect of LN (which acts in the opposite direction of the thermo-optic effect) permits the soliton mode-locking process to self-start and, more importantly, makes switching between the soliton states possible through both up- and down-tuning of the laser frequency. In a very similar work, operating around  $\lambda = 2 \mu\text{m}$  to reduce the impact of stimulated Raman scattering (SRS) on Kerr comb generation, Gong et al.<sup>164</sup> illustrated a line spacing of  $\sim 200$  GHz over a span of  $\sim 300$  nm. Wang et al.<sup>165</sup> made an integrated chip with filters and modulators to manipulate the output of the generated OFC. They designed a microring resonator capable of supporting both TE and TM polarizations with anomalous dispersion for both cases and reported on OFC generation spanning over 700 and 300 nm for TE and TM polarizations, respectively, with  $\sim 250$  GHz spacing. However, the soliton state was not achieved, and the generated combs were attributed to modulation instability due to the Raman effect. Therefore, the strong Raman effect needs to be

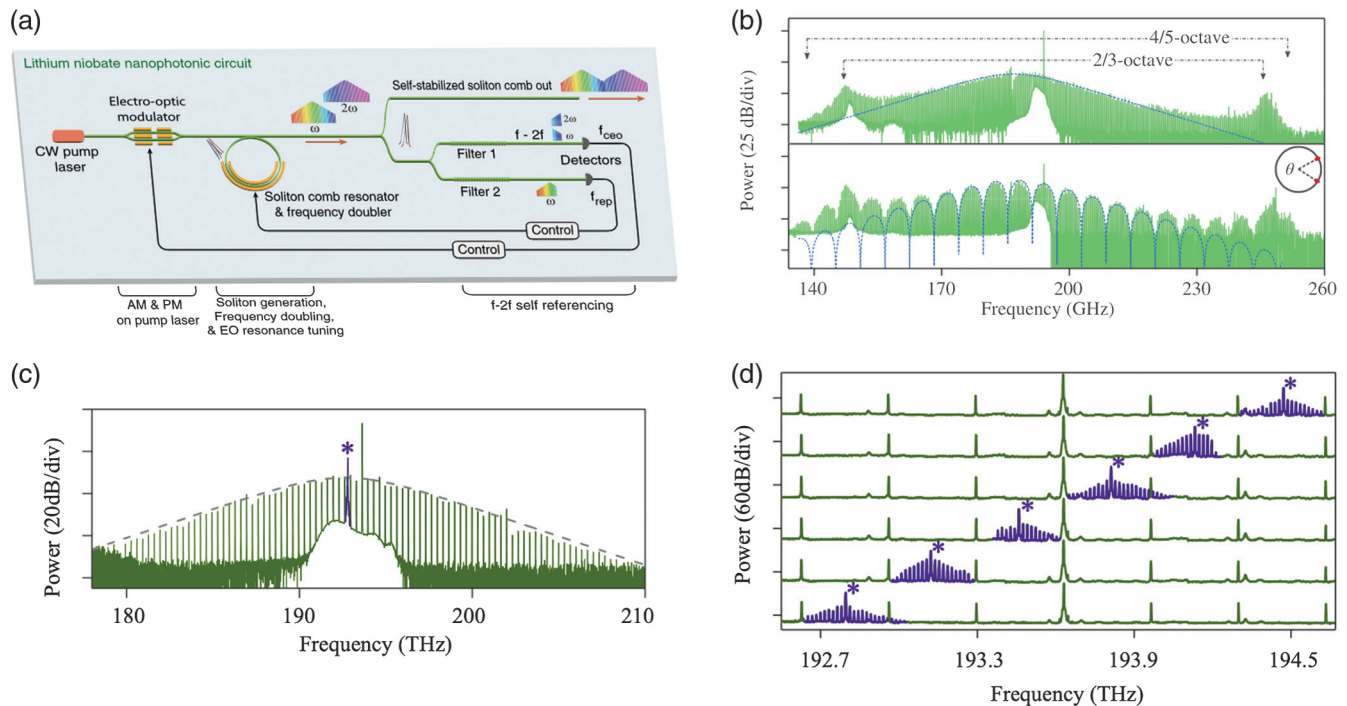


**Fig. 8** OFC generation in TFLN using the Kerr effect. (a) Conceptual schematic of a fully integrated soliton comb system in TFLN with all the required functionalities.<sup>161</sup> (b) Soliton Kerr comb generation spanning near one octave.<sup>162</sup> (c) Cascaded Kerr and EO combs with green lines corresponding to Kerr comb lines spanning over 200 nm.<sup>163</sup> (d) Zoomed in spectra of the cascaded Kerr and EO combs demonstrating that EO combs with much lower repetition rates fill the gap between Kerr combs.<sup>163</sup>

circumvented to have frequency combs in soliton states. Gong et al.<sup>162</sup> accomplished this goal by increasing the threshold energy for SRS to more than that of the soliton through a delicate design of the external coupling rate with respect to the intrinsic decay rate. As a result, soliton frequency combs spanning over 4/5 octaves, with a spacing of  $\sim 335$  GHz, were demonstrated [see Fig. 8(b)]. Pushing the span over an octave enables highly desired  $f - 2f$  self-referencing for this type of OFCs on the TFLN platform. It should be noted that the conversion efficiency from pump to comb lines is currently low for practical applications and further improvements are required for on-chip Kerr combs. The same group recently demonstrated a cascaded Kerr and EO comb, where the EO comb lines with much lower repetition rates filled the gap between Kerr soliton combs [Figs. 8(c) and 8(d)].<sup>163</sup> In addition, this could facilitate the stabilization of Kerr combs.

## 4 Conclusions and Outlook

Some of the initial research studies and recent developments in nonlinear photonics on the TFLN platform were reviewed. The improvements are magnificent for such a relatively short period of time, reaching or surpassing the performance of prior platforms for nonlinear applications. Despite outstanding demonstrated performances, this platform is still in its early years of development and will have a lot more to offer in the future.

There is plenty of room left for improvement of the TFLN platform before it becomes a fully functional integrated photonic platform. Fabrication needs to ultimately reach a point that reproducible, high-yield, and wafer-scale processing can be

accomplished in foundries, while pushing the propagation losses down to the material absorption limit.

There are more essential photonic components that must be incorporated to the platform either monolithically or through heterogeneous integration. As mentioned before, progress has been made in heterogeneously integrated semiconductor lasers in TFLN.<sup>32,33</sup> Similar methods could be adopted for integration of semiconductor photodetectors on this platform. Other examples include cointegration of second- and third-order materials. As discussed, LN has a relatively high third-order Kerr optical susceptibility. But in some applications, such as OFCs, it is still sensible to utilize other materials—such as SiN or chalcogenide glass—that may be advantageous in terms of nonlinear coefficient, optical loss, dispersion management, cost, compatibility with silicon foundry fabrication, etc. To this end, our team and collaborators have made progress in heterogeneous integration of TFLN and chalcogenide glass waveguides on the same silicon substrates.<sup>166,167</sup>

Furthermore, besides improving the performance of devices based on different optical and other functionalities (e.g., EO, second- and third-order nonlinearities and piezoelectricity), all of them may need to be integrated on the same chip to fully utilize the capabilities of this versatile platform.

A lot of further milestones can be accomplished for nonlinear photonics on TFLN. Material properties, such as the photo-refractive effect, need to be more accurately studied. For second-order nonlinearities, QPM using periodic poling still appears to be the most efficient method. The poling process can be perfected and standardized at the foundry level to achieve

high-yield and high-performance PPLN devices with  $<100$  nm poling periods. Such small poling periods compensate for large phase mismatches, which can be very functional especially for counterpropagating QPM processes. With the reported performances for PPLN microring devices and considering their small footprint and low power consumption, they could be promising devices for  $\chi^{(2)}$  processes in certain applications. However, one caveat for PPLN microrings is that the most efficient devices are made on Z-cut TFLN and operate in the TM polarization, which may not be the best option for ultimate fully integrated chips since the output of semiconductor lasers is usually TE-polarized, thus on-chip TE-to-TM polarization rotators will be required. Nonetheless, passive on-chip TM-to-TE polarization rotators<sup>168</sup> and polarization rotator-splitters<sup>169,170</sup> have been recently reported in TFLN. It is expected that reliable, low-loss, and high extinction ratio passive TE-to-TM polarization rotators will be demonstrated in the platform in the future. Furthermore, and as mentioned before, straight-waveguide PPLNs can typically handle higher powers and are more tolerant to fabrication errors and environmental fluctuations.

On-chip amplification in TFLN has been accomplished using heterogeneously integrated semiconductor optical amplifiers,<sup>32</sup> Er-doped amplifiers,<sup>171–173</sup> and OPAs.<sup>123,124</sup> Cascaded  $\chi^{(2)}$  processes are anticipated to be much more sophisticated than can be used for efficient frequency conversion in the ultraviolet and mid-IR wavelength ranges as well as generating broadband OFC and SCG sources. The current high demand for OFCs, along with the miniaturization and robustness that comes with integrated OFC on the TFLN platform, will push the limits for this type of devices to have higher conversion efficiencies and SNR with self-referencing incorporated in them. Also, EO devices are envisioned to be effectively integrated with all types of nonlinear devices for fast tuning or high-speed modulation.

Finally, considering the current progress in the efficiency of nonlinear processes, especially second-order effects, it is expected to achieve very high absolute conversion efficiencies in the future. Reaching large values in absolute efficiency will be a major step forward for integrated nonlinear photonics and its applications. Integrated quantum photonics will be severely pursued at that point since nonlinearity at the single photon level will be accessible.

In summary, TFLN has emerged as a mature platform for integrated photonics on a ferro-electric material with high second- and third-order nonlinearity. The high-contrast and low-loss waveguides on TFLN make them ideal for realization of compact nonlinear devices operating at low powers compared with conventional waveguides on the same material or on other materials. Several applications, such as optical spectroscopy, wavelength conversion for light generation at inconvenient wavelengths, digital optical synthesizers, and quantum optics, can be realized using the discussed efficient nonlinear devices and circuits on TFLN.

### Acknowledgments

Some of the results by the authors' group were funded by Office of Naval Research (N000141712409); Division of Emerging Frontiers in Research and Innovation (1741694) and under the Defense Advanced Research Project Agency (DARPA) DODOS project, Grant No. HR0011-15-C-0057. The views, opinions, and/or findings expressed are those of the authors and should not be interpreted as representing the official

views or policies of the Department of Defense or the U.S. Government. The authors have no conflicts of interest to disclose.

### References

1. N. Uesugi and T. Kimura, "Efficient second-harmonic generation in three-dimensional LiNbO<sub>3</sub> optical waveguide," *Appl. Phys. Lett.* **29**(9), 572–574 (1976).
2. R. Schmidt and I. Kaminow, "Metal-diffused optical waveguides in LiNbO<sub>3</sub>," *Appl. Phys. Lett.* **25**(8), 458–460 (1974).
3. J. L. Jackel, C. Rice, and J. Veselka, "Proton exchange for high-index waveguides in LiNbO<sub>3</sub>," *Appl. Phys. Lett.* **41**(7), 607–608 (1982).
4. P. Rabiei et al., "Heterogeneous lithium niobate photonics on silicon substrates," *Opt. Express* **21**(21), 25573–25581 (2013).
5. Partow Technologies, LLC, <http://www.partow-tech.com/> (accessed: March 2022).
6. NanoLN, <http://www.nanoln.com/> (accessed: March 2022).
7. Ngk insulators, Ltd., <https://www.ngk-insulators.com/> (accessed March 2022).
8. Y. Kong et al., "Recent progress in lithium niobate: optical damage, defect simulation, and on-chip devices," *Adv. Mater.* **32**(3), 1806452 (2020).
9. Y. Xu et al., "Mitigating photorefractive effect in thin-film lithium niobate microring resonators," *Opt. Express* **29**(4), 5497–5504 (2021).
10. A. L. Kozub et al., "Polaronic enhancement of second-harmonic generation in lithium niobate," *Phys. Rev. B* **104**(17), 174110 (2021).
11. M. Boukhtouta et al., "Predictions on structural, electronic, optical and thermal properties of lithium niobate via first-principle computations," *Philos. Mag.* **100**(9), 1150–1171 (2020).
12. A. Rao et al., "Heterogeneous microring and Mach-Zehnder modulators based on lithium niobate and chalcogenide glasses on silicon," *Opt. Express* **23**(17), 22746–22752 (2015).
13. A. Rao et al., "Second-harmonic generation in periodically-poled thin film lithium niobate wafer-bonded on silicon," *Opt. Express* **24**(26), 29941–29947 (2016).
14. A. Honardoost et al., "Towards subterahertz bandwidth ultra-compact lithium niobate electrooptic modulators," *Opt. Express* **27**(5), 6495–6501 (2019).
15. M. Zhang et al., "Monolithic ultra-high- $Q$  lithium niobate microring resonator," *Optica* **4**(12), 1536–1537 (2017).
16. R. Gao et al., "Broadband highly efficient nonlinear optical processes in on-chip integrated lithium niobate microdisk resonators of  $Q$ -factor above  $10^8$ ," *New J. Phys.* **23**(12), 123027 (2021).
17. K. Luke et al., "Wafer-scale low-loss lithium niobate photonic integrated circuits," *Opt. Express* **28**(17), 24452–24458 (2020).
18. J. Lin et al., "Advances in on-chip photonic devices based on lithium niobate on insulator," *Photonics Res.* **8**(12), 1910–1936 (2020).
19. Y. Jia, L. Wang, and F. Chen, "Ion-cut lithium niobate on insulator technology: recent advances and perspectives," *Appl. Phys. Rev.* **8**(1), 011307 (2021).
20. D. Sun et al., "Microstructure and domain engineering of lithium niobate crystal films for integrated photonic applications," *Light: Sci. Appl.* **9**(1), 197 (2020).
21. Y. Jiao et al., "Improvement on thermal stability of nano-domains in lithium niobate thin films," *Crystals* **10**(2), 74 (2020).
22. M. Younesi et al., "Periodic poling with a micrometer-range period in thin-film lithium niobate on insulator," *J. Opt. Soc. Am. B* **38**(3), 685–691 (2021).
23. B. J. Stanicki et al., "Surface domain engineering in lithium niobate," *OSA Contin.* **3**(2), 345–358 (2020).
24. Y. Liu et al., "On-chip erbium-doped lithium niobate microcavity laser," *Sci. China Phys. Mech. Astron.* **64**(3), 234262 (2021).

25. R. Gao et al., "On-chip ultra-narrow-linewidth single-mode microlaser on lithium niobate on insulator," *Opt. Lett.* **46**(13), 3131–3134 (2021).
26. Q. Luo et al., "On-chip erbium-doped lithium niobate microring lasers," *Opt. Lett.* **46**(13), 3275–3278 (2021).
27. X. Liu et al., "Tunable single-mode laser on thin film lithium niobate," *Opt. Lett.* **46**(21), 5505–5508 (2021).
28. D. Yin et al., "Electro-optically tunable microring laser monolithically integrated on lithium niobate on insulator," *Opt. Lett.* **46**(9), 2127–2130 (2021).
29. R. Zhang et al., "Integrated lithium niobate single-mode lasers by the Vernier effect," *Sci. China Phys. Mech. Astron.* **64**(9), 294216 (2021).
30. M. Yu et al., "Raman lasing and soliton mode-locking in lithium niobate microresonators," *Light: Sci. Appl.* **9**(1), 9 (2020).
31. D. Zhu et al., "Integrated photonics on thin-film lithium niobate," *Adv. Opt. Photonics* **13**(2), 242–352 (2021).
32. C. O. de Beeck et al., "III/V-on-lithium niobate amplifiers and lasers," *Optica* **8**(10), 1288–1289 (2021).
33. A. Shams-Ansari et al., "Electrically pumped laser transmitter integrated on thin-film lithium niobate," *Optica* **9**(4), 408–411 (2022).
34. A. Honardoost, K. Abdelsalam, and S. Fathpour, "Rejuvenating a versatile photonic material: thin-film lithium niobate," *Laser Photonics Rev.* **14**(9), 2000088 (2020).
35. Y. Qi and Y. Li, "Integrated lithium niobate photonics," *Nanophotonics* **9**(6), 1287–1320 (2020).
36. M. Xu et al., "Dual-polarization thin-film lithium niobate in-phase quadrature modulators for terabit-per-second transmission," *Optica* **9**(1), 61–62 (2022).
37. F. Arab Juneghani et al., "Demonstration of non-symmetric thin-film lithium niobate modulator with a 3-dB bandwidth beyond 100 GHz," in *CLEO: Sci. and Innov.*, Optical Society of America (2022).
38. C. Hu et al., "High-efficient coupler for thin-film lithium niobate waveguide devices," *Opt. Express* **29**(4), 5397–5406 (2021).
39. K. Abdelsalam et al., "Tunable dual-channel ultra-narrowband Bragg grating filter on thin-film lithium niobate," *Opt. Lett.* **46**(11), 2730–2733 (2021).
40. K. Abdelsalam et al., "Linear isolators using wavelength conversion," *Optica* **7**(3), 209–213 (2020).
41. X. Ye et al., "High-speed programmable lithium niobate thin film spatial light modulator," *Opt. Lett.* **46**(5), 1037–1040 (2021).
42. P. Franken et al., "Generation of optical harmonics," *Phys. Rev. Lett.* **7**(4), 118–119 (1961).
43. R. W. Boyd, *Nonlinear Optics*, Academic Press (2020).
44. A. Rao and S. Fathpour, "Second-harmonic generation in integrated photonics on silicon," *Phys. Status Solidi A* **215**(4), 1700684 (2018).
45. A. Rao and S. Fathpour, "Heterogeneous thin-film lithium niobate integrated photonics for electrooptics and nonlinear optics," *IEEE J. Sel. Top. Quantum Electron.* **24**(6), 8200912 (2018).
46. S. Fathpour, "Heterogeneous nonlinear integrated photonics," *IEEE J. Quantum Electron.* **54**(6), 6300776 (2018).
47. W. H. P. Pernice et al., "Second harmonic generation in phase matched aluminium nitride waveguides and micro-ring resonators," *Appl. Phys. Lett.* **100**(22), 223501 (2012).
48. S. May et al., "Second-harmonic generation in AlGaAs-on-insulator waveguides," *Opt. Lett.* **44**(6), 1339–1342 (2019).
49. L. Chang et al., "Heterogeneously integrated GaAs waveguides on insulator for efficient frequency conversion," *Laser Photonics Rev.* **12**(10), 1800149 (2018).
50. C. Xiong et al., "Integrated GaN photonic circuits on silicon (100) for second harmonic generation," *Opt. Express* **19**(11), 10462–10470 (2011).
51. D. N. Nikogosyan, *Nonlinear Optical Crystals: A Complete Survey*, Springer Science & Business Media (2006).
52. N. Li et al., "Aluminium nitride integrated photonics: a review," *Nanophotonics* **10**, 2347–2387 (2021).
53. H. Zhang et al., "Study of nonlinear optical effects in GaN: Mg epitaxial film," *Appl. Phys. Lett.* **69**(20), 2953–2955 (1996).
54. J. Webjorn, F. Laurell, and G. Arvidsson, "Fabrication of periodically domain-inverted channel waveguides in lithium niobate for second harmonic generation," *J. Lightwave Technol.* **7**(10), 1597–1600 (1989).
55. E. Lim, M. Fejer, and R. Byer, "Second-harmonic generation of green light in periodically poled planar lithium niobate waveguide," *Electron. Lett.* **25**(3), 174–175 (1989).
56. L. E. Myers et al., "Multigrating quasi-phase-matched optical parametric oscillator in periodically poled LiNbO<sub>3</sub>," *Opt. Lett.* **21**(8), 591–593 (1996).
57. G. Miller et al., "42%-efficient single-pass CW second-harmonic generation in periodically poled lithium niobate," *Opt. Lett.* **22**(24), 1834–1836 (1997).
58. S. Fathpour, "Emerging heterogeneous integrated photonic platforms on silicon," *Nanophotonics* **4**(1), 143–164 (2015).
59. C. Lu et al., "Highly tunable birefringent phase-matched second-harmonic generation in an angle-cut lithium niobate-on-insulator ridge waveguide," *Opt. Lett.* **47**(5), 1081–1084 (2022).
60. R. Luo et al., "Optical parametric generation in a lithium niobate microring with modal phase matching," *Phys. Rev. Appl.* **11**(3), 034026 (2019).
61. A. Rao et al., "Second-harmonic generation in single-mode integrated waveguides based on mode-shape modulation," *Appl. Phys. Lett.* **110**(11), 111109 (2017).
62. J. Lin et al., "Broadband quasi-phase-matched harmonic generation in an on-chip monocrystalline lithium niobate microdisk resonator," *Phys. Rev. Lett.* **122**(17), 173903 (2019).
63. C. Wang et al., "Metasurface-assisted phase-matching-free second harmonic generation in lithium niobate waveguides," *Nat. Commun.* **8**(1), 2098 (2017).
64. C. Wang et al., "Second harmonic generation in nano-structured thin-film lithium niobate waveguides," *Opt. Express* **25**(6), 6963–6973 (2017).
65. R. Luo et al., "Highly tunable efficient second-harmonic generation in a lithium niobate nanophotonic waveguide," *Optica* **5**(8), 1006–1011 (2018).
66. J.-Y. Chen et al., "Modal phase matched lithium niobate nanocircuits for integrated nonlinear photonics," *OSA Contin.* **1**(1), 229–242 (2018).
67. R. Luo et al., "Semi-nonlinear nanophotonic waveguides for highly efficient second-harmonic generation," *Laser Photonics Rev.* **13**(3), 1800288 (2019).
68. C. Wang et al., "Integrated high quality factor lithium niobate microdisk resonators," *Opt. Express* **22**(25), 30924–30933 (2014).
69. S. Liu, Y. Zheng, and X. Chen, "Cascading second-order nonlinear processes in a lithium niobate-on-insulator microdisk," *Opt. Lett.* **42**(18), 3626–3629 (2017).
70. S. Liu et al., "Effective four-wave mixing in the lithium niobate on insulator microdisk by cascading quadratic processes," *Opt. Lett.* **44**(6), 1456–1459 (2019).
71. E. Lim et al., "Blue light generation by frequency doubling in periodically poled lithium niobate channel waveguide," *Electron. Lett.* **25**(11), 731–732 (1989).
72. L. E. Myers et al., "Quasi-phase-matched optical parametric oscillators in bulk periodically poled LiNbO<sub>3</sub>," *J. Opt. Soc. Am. B* **12**(11), 2102–2116 (1995).
73. L. Chang et al., "Thin film wavelength converters for photonic integrated circuits," *Optica* **3**(5), 531–535 (2016).
74. J. T. Nagy and R. M. Reano, "Reducing leakage current during periodic poling of ion-sliced x-cut MgO doped lithium niobate thin films," *Opt. Mater. Express* **9**(7), 3146–3155 (2019).
75. A. Boes et al., "Efficient second harmonic generation in lithium niobate on insulator waveguides and its pitfalls," *J. Phys.: Photonics* **3**(1), 012008 (2021).

76. J. Zhao et al., "Poling thin-film x-cut lithium niobate for quasi-phase matching with sub-micrometer periodicity," *J. Appl. Phys.* **127**(19), 193104 (2020).
77. B. Slautin et al., "Domain structure formation by local switching in the ion sliced lithium niobate thin films," *Appl. Phys. Lett.* **116**(15), 152904 (2020).
78. J. T. Nagy and R. M. Reano, "Submicrometer periodic poling of lithium niobate thin films with bipolar preconditioning pulses," *Opt. Mater. Express* **10**(8), 1911–1920 (2020).
79. S. Reitzig et al., "“Seeing is believing” —in-depth analysis by co-imaging of periodically-poled x-cut lithium niobate thin films," *Crystals* **11**(3), 288 (2021).
80. R. K. Prasath et al., "Measurement of the internal electric field in periodically poled congruent lithium niobate crystals by far-field diffraction," *Appl. Opt.* **60**(13), 3791–3796 (2021).
81. A. Boes et al., "Improved second harmonic performance in periodically poled LNOI waveguides through engineering of lateral leakage," *Opt. Express* **27**(17), 23919–23928 (2019).
82. A. Rao et al., "Actively-monitored periodic-poling in thin-film lithium niobate photonic waveguides with ultrahigh nonlinear conversion efficiency of  $4600\% \text{ W}^{-1} \text{ cm}^{-2}$ ," *Opt. Express* **27**(18), 25920–25930 (2019).
83. J.-Y. Chen et al., "Ultra-efficient frequency conversion in quasi-phase-matched lithium niobate microrings," *Optica* **6**(9), 1244–1245 (2019).
84. J. Lu et al., "Toward 1% single-photon anharmonicity with periodically poled lithium niobate microring resonators," *Optica* **7**(12), 1654–1659 (2020).
85. Z. Hao et al., "Second-harmonic generation using  $d_{33}$  in periodically poled lithium niobate microdisk resonators," *Photonics Res.* **8**(3), 311–317 (2020).
86. C. Wang et al., "Ultrahigh-efficiency wavelength conversion in nanophotonic periodically poled lithium niobate waveguides," *Optica* **5**(11), 1438–1441 (2018).
87. J.-Y. Chen et al., "Efficient parametric frequency conversion in lithium niobate nanophotonic chips," *OSA Contin.* **2**(10), 2914–2924 (2019).
88. J. Zhao et al., "Shallow-etched thin-film lithium niobate waveguides for highly-efficient second-harmonic generation," *Opt. Express* **28**(13), 19669–19682 (2020).
89. C. Lu et al., "Second and cascaded harmonic generation of pulsed laser in a lithium niobate on insulator ridge waveguide," *Opt. Express* **30**(2), 1381–1387 (2022).
90. J. Lu et al., "Periodically poled thin-film lithium niobate microring resonators with a second-harmonic generation efficiency of  $250,000\%/W$ ," *Optica* **6**(12), 1455–1460 (2019).
91. J. Lin et al., "Phase-matched second-harmonic generation in an on-chip LiNbO<sub>3</sub> microresonator," *Phys. Rev. Appl.* **6**(1), 014002 (2016).
92. M. Li et al., "Photon-photon quantum phase gate in a photonic molecule with  $\chi^{(2)}$  nonlinearity," *Phys. Rev. Appl.* **13**(4), 044013 (2020).
93. M. Heuck, K. Jacobs, and D. R. Englund, "Controlled-phase gate using dynamically coupled cavities and optical nonlinearities," *Phys. Rev. Lett.* **124**(16), 160501 (2020).
94. R. Wolf et al., "Quasi-phase-matched nonlinear optical frequency conversion in on-chip whispering galleries," *Optica* **5**(7), 872–875 (2018).
95. L. Zhang et al., "Dual-periodically poled lithium niobate microcavities supporting multiple coupled parametric processes," *Opt. Lett.* **45**(12), 3353–3356 (2020).
96. G. Lin et al., "Wide-range cyclic phase matching and second harmonic generation in whispering gallery resonators," *Appl. Phys. Lett.* **103**(18), 181107 (2013).
97. R. Luo et al., "On-chip second-harmonic generation and broadband parametric down-conversion in a lithium niobate microresonator," *Opt. Express* **25**(20), 24531–24539 (2017).
98. R. Wu et al., "Lithium niobate micro-disk resonators of quality factors above  $10^7$ ," *Opt. Lett.* **43**(17), 4116–4119 (2018).
99. A. Fedotova et al., "Second-harmonic generation in resonant nonlinear metasurfaces based on lithium niobate," *Nano Lett.* **20**(12), 8608–8614 (2020).
100. J. Ma et al., "Nonlinear lithium niobate metasurfaces for second harmonic generation," *Laser Photonics Rev.* **15**(5), 2000521 (2021).
101. Y. Li et al., "Optical anapole mode in nanostructured lithium niobate for enhancing second harmonic generation," *Nanophotonics* **9**(11), 3575–3585 (2020).
102. F. Renaud et al., "Second-harmonic-generation enhancement in cavity resonator integrated grating filters," *Opt. Lett.* **44**(21), 5198–5201 (2019).
103. S. Yuan et al., "Strongly enhanced second harmonic generation in a thin film lithium niobate heterostructure cavity," *Phys. Rev. Lett.* **127**(15), 153901 (2021).
104. Y. Li et al., "Recent progress of second harmonic generation based on thin film lithium niobate," *Chin. Opt. Lett.* **19**(6), 060012 (2021).
105. H. Jiang et al., "Nonlinear frequency conversion in one dimensional lithium niobate photonic crystal nanocavities," *Appl. Phys. Lett.* **113**(2), 021104 (2018).
106. M. Li et al., "High- $Q$  2D lithium niobate photonic crystal slab nanoresonators," *Laser Photonics Rev.* **13**(5), 1800228 (2019).
107. J. S. Dam, P. Tidemand-Lichtenberg, and C. Pedersen, "Room-temperature mid-infrared single-photon spectral imaging," *Nat. Photonics* **6**(11), 788–793 (2012).
108. G. Li et al., "Broadband sum-frequency generation using  $d_{33}$  in periodically poled LiNbO<sub>3</sub> thin film in the telecommunications band," *Opt. Lett.* **42**(5), 939–942 (2017).
109. Z. Hao et al., "Sum-frequency generation in on-chip lithium niobate microdisk resonators," *Photonics Res.* **5**(6), 623–628 (2017).
110. X. Ye et al., "Sum-frequency generation in lithium-niobate-on-insulator microdisk via modal phase matching," *Opt. Lett.* **45**(2), 523–526 (2020).
111. A. K. Hansen et al., "Highly efficient single-pass sum frequency generation by cascaded nonlinear crystals," *Opt. Lett.* **40**(23), 5526–5529 (2015).
112. T. Sjaardema, A. Rao, and S. Fathpour, "Third- and fourth-harmonic generation in cascaded periodically-poled lithium niobate ultracompact waveguides on silicon," in *CLEO: Sci. and Innov.*, Optical Society of America, p. STh1J-1 (2019).
113. S. Lauria and M. F. Saleh, "Mixing second- and third-order nonlinear interactions in nanophotonic lithium-niobate waveguides," *Phys. Rev. A* **105**(4), 043511 (2021).
114. R. Wolf et al., "Cascaded second-order optical nonlinearities in on-chip micro rings," *Opt. Express* **25**(24), 29927–29933 (2017).
115. D. D. Hickstein et al., "High-harmonic generation in periodically poled waveguides," *Optica* **4**(12), 1538–1544 (2017).
116. D. Wang et al., "Cascaded sum-frequency generation and electro-optic polarization coupling in the PPLNOI ridge waveguide," *Opt. Express* **27**(11), 15283–15288 (2019).
117. Y. J. Ding, "Progress in terahertz sources based on difference-frequency generation," *J. Opt. Soc. Am. B* **31**(11), 2696–2711 (2014).
118. C. Erny et al., "Mid-infrared difference-frequency generation of ultrashort pulses tunable between 3.2 and 4.8  $\mu\text{m}$  from a compact fiber source," *Opt. Lett.* **32**(9), 1138–1140 (2007).
119. J. Mishra et al., "Mid-infrared nonlinear optics in thin-film lithium niobate on sapphire," *Optica* **8**(6), 921–924 (2021).
120. J. Yang and C. Wang, "Efficient terahertz generation scheme in a thin-film lithium niobate-silicon hybrid platform," *Opt. Express* **29**(11), 16477–16486 (2021).
121. F. Kaufmann et al., "On-chip optical parametric amplification in subwavelength lithium niobate nanowaveguides," in *Integr.*

- Photonics Res., Silicon and Nanophotonics*, Optical Society of America, p. JTu5A-52 (2018).
122. J.-Y. Chen et al., "Phase-sensitive amplification in nanophotonic periodically poled lithium niobate waveguides," in *CLEO: Sci. and Innov.*, Optical Society of America, p. SM3L-5 (2020).
  123. L. Ledezma et al., "Intense optical parametric amplification in dispersion engineered nanophotonic lithium niobate waveguides," arXiv:2104.08262 (2021).
  124. M. Jankowski et al., "Quasi-static optical parametric amplification," *Optica* **9**(3), 273–279 (2022).
  125. J. Lu et al., "Ultralow-threshold thin-film lithium niobate optical parametric oscillator," *Optica* **8**(4), 539–544 (2021).
  126. D. C. Burnham and D. L. Weinberg, "Observation of simultaneity in parametric production of optical photon pairs," *Phys. Rev. Lett.* **25**(2), 84–87 (1970).
  127. T. Jennewein et al., "Quantum cryptography with entangled photons," *Phys. Rev. Lett.* **84**(20), 4729–4732 (2000).
  128. D. Bouwmeester et al., "Experimental quantum teleportation," *Nature* **390**(6660), 575–579 (1997).
  129. B. S. Elkus et al., "Generation of broadband correlated photon-pairs in short thin-film lithium-niobate waveguides," *Opt. Express* **27**(26), 38521–38531 (2019).
  130. B. S. Elkus et al., "Quantum-correlated photon-pair generation via cascaded nonlinearity in an ultra-compact lithium-niobate nano-waveguide," *Opt. Express* **28**(26), 39963–39975 (2020).
  131. G.-T. Xue et al., "Ultrabright multiplexed energy-time-entangled photon generation from lithium niobate on insulator chip," *Phys. Rev. Appl.* **15**(6), 064059 (2021).
  132. J. Zhao et al., "High quality entangled photon pair generation in periodically poled thin-film lithium niobate waveguides," *Phys. Rev. Lett.* **124**(16), 163603 (2020).
  133. U. A. Javid et al., "Ultrabroadband entangled photons on a nanophotonic chip," *Phys. Rev. Lett.* **127**(18), 183601 (2021).
  134. Z. Ma et al., "Ultrabright quantum photon sources on chip," *Phys. Rev. Lett.* **125**(26), 263602 (2020).
  135. S. Saravi, T. Pertsch, and F. Setzpfandt, "Lithium niobate on insulator: an emerging platform for integrated quantum photonics," *Adv. Opt. Mater.* **9**(22), 2100789 (2021).
  136. G. I. Stegeman, D. J. Hagan, and L. Torner, " $\chi^{(2)}$  cascading phenomena and their applications to all-optical signal processing, mode-locking, pulse compression and solitons," *Opt. Quantum Electron.* **28**(12), 1691–1740 (1996).
  137. T. Sjaardema et al., "Low-harmonic generation in cascaded thin-film lithium niobate waveguides," *Adv. Photonics Res.* **2022**, 2100262 (2022).
  138. M. Wang et al., "Strong nonlinear optics in on-chip coupled lithium niobate microdisk photonic molecules," *New J. Phys.* **22**(7), 073030 (2020).
  139. M. Jankowski et al., "Ultrabroadband nonlinear optics in nanophotonic periodically poled lithium niobate waveguides," *Optica* **7**(1), 40–46 (2020).
  140. M. Malinowski et al., "Towards on-chip self-referenced frequency-comb sources based on semiconductor mode-locked lasers," *Micromachines* **10**(6), 391 (2019).
  141. S. Mosca et al., "Modulation instability induced frequency comb generation in a continuously pumped optical parametric oscillator," *Phys. Rev. Lett.* **121**(9), 093903 (2018).
  142. A. W. Bruch et al., "Pockels soliton microcomb," *Nat. Photonics* **15**(1), 21–27 (2021).
  143. R. Ikuta et al., "Frequency comb generation in a quadratic nonlinear waveguide resonator," *Opt. Express* **26**(12), 15551–15558 (2018).
  144. X. Wang et al., " $2\ \mu\text{m}$  optical frequency comb generation via optical parametric oscillation from a lithium niobate optical superlattice box resonator," *Photonics Res.* **10**(2), 509–515 (2022).
  145. N. Amiune et al., "Optical-parametric-oscillation-based  $\chi^{(2)}$  frequency comb in a lithium niobate microresonator," *Opt. Express* **29**(25), 41378–41387 (2021).
  146. I. Hendry et al., "Experimental observation of internally pumped parametric oscillation and quadratic comb generation in a  $\chi^{(2)}$  whispering-gallery-mode microresonator," *Opt. Lett.* **45**(5), 1204–1207 (2020).
  147. J. Szabados et al., "Frequency comb generation via cascaded second-order nonlinearities in microresonators," *Phys. Rev. Lett.* **124**(20), 203902 (2020).
  148. Y. Hu et al., "High-efficiency and broadband electro-optic frequency combs enabled by coupled micro-resonators," arXiv:2111.14743 (2021).
  149. T. Ren et al., "An integrated low-voltage broadband lithium niobate phase modulator," *IEEE Photonics Technol. Lett.* **31**(11), 889–892 (2019).
  150. M. Xu et al., "Integrated lithium niobate modulator and frequency comb generator based on Fabry-Perot resonators," in *CLEO: Appl. and Technol.*, Optical Society of America, p. JTh2B-27 (2020).
  151. M. Zhang et al., "Broadband electro-optic frequency comb generation in a lithium niobate microring resonator," *Nature* **568**(7752), 373–377 (2019).
  152. H. Sun et al., "Recent progress in integrated electro-optic frequency comb generation," *J. Semicond.* **42**(4), 041301 (2021).
  153. R. Normandin and G. I. Stegeman, "Nondegenerate four-wave mixing in integrated optics," *Opt. Lett.* **4**(2), 58–59 (1979).
  154. B. J. Eggleton et al., "Brillouin integrated photonics," *Nat. Photonics* **13**(10), 664–677 (2019).
  155. R. Loudon, "The Raman effect in crystals," *Adv. Phys.* **13**(52), 423–482 (1964).
  156. L. Cai et al., "Acousto-optical modulation of thin film lithium niobate waveguide devices," *Photonics Res.* **7**(9), 1003–1013 (2019).
  157. A. L. Gaeta, M. Lipson, and T. J. Kippenberg, "Photonic-chip-based frequency combs," *Nat. Photonics* **13**(3), 158–169 (2019).
  158. Y. Okawachi et al., "Chip-based self-referencing using integrated lithium niobate waveguides," *Optica* **7**(6), 702–707 (2020).
  159. M. Yu et al., "Coherent two-octave-spanning supercontinuum generation in lithium-niobate waveguides," *Opt. Lett.* **44**(5), 1222–1225 (2019).
  160. J. Lu et al., "Octave-spanning supercontinuum generation in nanoscale lithium niobate waveguides," *Opt. Lett.* **44**(6), 1492–1495 (2019).
  161. Y. He et al., "Self-starting bi-chromatic LiNbO<sub>3</sub> soliton microcomb," *Optica* **6**(9), 1138–1144 (2019).
  162. Z. Gong et al., "Near-octave lithium niobate soliton microcomb," *Optica* **7**(10), 1275–1278 (2020).
  163. Z. Gong et al., "Monolithic Kerr and electro-optic hybrid microcombs," arXiv:2202.02920 (2022).
  164. Z. Gong et al., "Soliton microcomb generation at  $2\ \mu\text{m}$  in z-cut lithium niobate microring resonators," *Opt. Lett.* **44**(12), 3182–3185 (2019).
  165. C. Wang et al., "Monolithic lithium niobate photonic circuits for Kerr frequency comb generation and modulation," *Nat. Commun.* **10**(1), 978 (2019).
  166. A. Honardoost et al., "Cascaded integration of optical waveguides with third-order nonlinearity with lithium niobate waveguides on silicon substrates," *IEEE Photonics J.* **10**(3), 4500909 (2018).
  167. G. F. C. Gonzalez et al., "Design of a hybrid chalcogenide-glass on lithium-niobate waveguide structure for high-performance cascaded third- and second-order optical nonlinearities," *Appl. Opt.* **58**(13), D1–D6 (2019).
  168. Y. Zhao et al., "Compact lithium-niobate-on-insulator polarization rotator based on asymmetric hybrid plasmonics waveguide," *IEEE Photonics J.* **13**(4), 4800105 (2021).
  169. Z. Chen et al., "Broadband adiabatic polarization rotator-splitter based on a lithium niobate on insulator platform," *Photonics Res.* **9**(12), 2319–2324 (2021).
  170. X. Wang et al., "Efficient polarization splitter-rotator on thin-film lithium niobate," *Opt. Express* **29**(23), 38044–38052 (2021).

171. M. Cai et al., "Erbium-doped lithium niobate thin film waveguide amplifier with 16 dB internal net gain," *IEEE J. Sel. Top. Quantum Electron.* **28**(3), 8200608 (2021).
172. Q. Luo et al., "On-chip erbium-doped lithium niobate waveguide amplifiers," *Chin. Opt. Lett.* **19**(6), 060008 (2021).
173. J. Zhou et al., "On-chip integrated waveguide amplifiers on erbium-doped thin-film lithium niobate on insulator," *Laser Photonics Rev.* **15**(8), 2100030 (2021).

**Milad Gholipour Vazimali** is a PhD candidate at CREOL, the College of Optics and Photonics at the University of Central Florida (UCF). He received his BS degree in electrical engineering from Sharif University of Technology in 2014. He received his first MS degree in semiconductor devices from the University of Tehran in 2017 and his second MS degree in optics from UCF in 2020. His current research interests include photonic integrated circuits, nonlinear optics, and optoelectronic devices.

**Sasan Fathpour** is a professor at CREOL, the College of Optics and Photonics at UCF with a secondary joint appointment at the Department of Electrical and Computer Engineering. He received his PhD in electrical engineering from the University of Michigan, Ann Arbor, in 2005. His current research interests include heterogeneous integrated photonics, nonlinear integrated optics, silicon photonics, and unconventional photonic platforms operating in the mid-wave- and near-infrared and visible wavelength ranges. He has received the US National Science Foundation CAREER Award (2012) and the Office of Naval Research Young Investigator Program Award (2013). He is a coauthor of over 190 publications, including about 80 journal papers, 6 book chapters, and 3 patents. He coedited the book *Silicon Photonics for Telecommunications and Biomedicine*, CRC Press (2012). He is the cofounder of Partow Technologies, LLC. He is an associate editor of *Optica* and has been a guest editor for the SPIE *Journal of Nanophotonics*. He is a fellow of *Optica*, a senior member of SPIE and IEEE, and a member of MRS.